MOLECULAR DYNAMICS STUDIES ON HEAT TRANSFER CONTROL BETWEEN WATER AND SILICA USING NANOSCALE SURFACE PATTERNS

A Thesis Submitted to
the Graduate School of Engineering and Science of
İzmir Institute of Technology
in Partial Fulfillment of the Requirements for the Degree of

MASTER OF SCIENCE

in Mechanical Engineering

by
Celal Can ÖZEN

December 2020
İZMİR

ACKNOWLEDGMENTS

I would like to express my gratitude to my advisor Assoc. Prof. Dr. Murat BARIŞIK for his endless motivation and support during my research and thesis. I am sincerely thankful to him for his academical experiences and knowledge. I am truly grateful for every second that I have worked with him.

As a part of MiNaEng (Micro/nano Engineering Research Group), I would like to thank several of my colleagues for their support and experiences. I would like to thank to Ezgi ŞATIROĞLU for her help and sharing her experience with me from the beginning of my studies. I would like to acknowledge my sincere gratitude to all my colleagues from the research group.

This work was supported by the Scientific and Technological Research Council of Turkey (TÜBİTAK) under Grant Number 217M460. I also thank for the support from the Turkish Academy of Sciences (TUBA) in the framework of the Young Scientist Award Programme (GEBIP). Also, I would like to thank to Turkish National e-Science e-Infrastructure (TRUBA), for providing us computational infrastructure to complete my researches.

Also, I would like to thank my loved ones, who supported me during my studies for their motivation and support. I will be grateful forever for your love.

ABSTRACT

MOLECULAR DYNAMICS STUDIES ON HEAT TRANSFER CONTROL BETWEEN WATER AND SILICA USING NANOSCALE SURFACE PATTERNS

Due to recent advances in manufacturing, component sizes have tremendously decreased in computer electronics and communication devices. Miniaturization has led to a substantial increase in memory and computational power but also created heat dissipation problems. Understanding heat transfer and temperature distribution in these devices became crucial for thermal management. At nanoscale, heat transfer through dielectric materials is mostly determined by phonon transport. The phonon passage is interrupted through the interfaces which creates temperature jumps and dominates the heat transfer rates at nanoscale. Kapitza length characterizes the interfacial thermal resistance as a function of temperature jump at the solid-liquid interface. In this study, heat transfer from different nanoscale surface structures were investigated using Molecular Dynamics simulations. The systems were created by two parallel silica walls and water between them. Kapitza length values were calculated for seven different surface conditions for two different molecular surface interaction strength parameters yielding high and low wetting conditions. Measured Kapitza length values were characterized based on cavity width (w), cavity height (h), and unit crystal cavity volume (V_c). While the increase in pattern cavity width increased Kapitza length, increasing pattern cavity height decreased Kapitza value. However, a general characterization based on cavity volume could not be obtained. Instead, almost a uniform behavior was observed through the variation of Kapitza length of different size patterns as a function of $A_c=V_ch/w^2$. Kapitza length decreased by approximately 19% and 29% for high and low wetting conditions, respectively, when A_c increased. Then, similar characterizations were done for variation of heat flux. Overall, heat flux increased by approximately 20% and 30% for high and low wetting conditions, respectively, when A_c increased. Results are important to better understand and control heat transfer between water and silica using nanoscale surface patterns.

Keywords: Nanoscale heat transfer, Solid-liquid interface, Molecular dynamics, Kapitza length, Heat flux

ÖZET

SU VE SİLİKA ARASINDAKİ ISI TRANSFERİNİN NANO-ÖLÇEK YÜZEY YAPILARI KULLANARAK KONTROLÜ ÜZERİNE MOLEKÜLER DİNAMİK ÇALIŞMALARI

Üretimdeki son gelişmeler nedeniyle, bilgisayar elektroniğinde ve iletişim cihazlarında parça boyutları büyük ölçüde azaldı. Minyatürleşme, bellek ve hesaplama gücünde önemli bir artışa yol açtı, ancak aynı zamanda ısı yayılımı sorunları yarattı. Bu cihazlarda ısı transferini ve sıcaklık dağılımını anlamak ısı yönetimi için çok önemli hale geldi. Nano ölçekte dielektrik malzemeler aracılığıyla ısı transferi çoğunlukla fonon taşınmasıyla belirlenir. Fonon geçişi, sıcaklık sıçramaları yaratan ve nano ölçekte ısı transfer oranlarına hakim olan arayüzler aracılığıyla kesintiye uğrar. Kapitza uzunluğu, arayüzey termal direncini katı-sıvı arayüzündeki sıcaklık sıçramasının bir fonksiyonu olarak karakterize eder. Bu çalışmada, farklı nano ölçekli yüzey yapılarındaki ısı transferi Moleküler Dinamik simulasyonları kullanılarak incelenmiştir. Sistemler, iki paralel silika duvar ve aralarında su ile oluşturuldu. Kapitza uzunluk değerleri, yüksek ve düşük ıslatma koşulları sağlayan iki farklı moleküler yüzey etkileşim kuvveti parametresi ve yedi farklı yüzey koşulu için hesaplanmıştır. Ölçülen Kapitza uzunluk değerleri, boşluk genişliği (w), boşluk yüksekliği (h), birim kristal boşluk hacmi (V_c) temelinde karakterize edildi. Model boşluğu genişliğindeki artış Kapitza uzunluğunu artırırken, artan model boşluğu yüksekliği Kapitza değerini düşürmüştür. Ancak boşluk hacmine dayalı genel bir karakterizasyon elde edilememiştir. Bunun yerine, $A_c=V_ch/w^2$'nin bir fonksiyonu olarak farklı boyut modellerinin Kapitza uzunluğunun varyasyonunda tek düze bir davranış gözlemlendi. Kapitza uzunluğu A_c arttığında yüksek ve düşük ıslatma durumlarında sırasıyla yaklaşık %19 ve %29 azalmıştır. Daha sonra ısı akısının değişimi için benzer karakterizasyonlar yapılmıştır. Genel olarak, ısı akısı, A_c arttığında yüksek ve düşük ıslatma durumları için sırasıyla yaklaşık %20 ve %30 artmıştır. Sonuçlar nano ölçekli yüzey modelleri kullanılarak su ve silika arasındaki ısı transferini daha iyi anlamak ve kontrol etmek için önemlidir.

Anahtar Kelimeler: Nano ölçekte ısı transferi, Katı-sıvı arayüzü, Moleküler dinamik, Kapitza uzunluğu, Isı akısı

TABLE OF CONTENTS

LIST OF FIGURES

Figure **Page**

Figure **Page**

LIST OF TABLES

LIST OF SYMBOLS

a	Acceleration	m/s^2
h	Cavity height	nm
w	Cavity width	nm
r	Intermolecular distance	nm
r(t)	Position	m
v(t)	Velocity	m/s
t	Time	s

Greek Letters

ε	Interaction strength, dielectric constant	eV, F/m
σ	Molecular diameter	Å
ρ	Density	g/cm^3

Subscripts

MD	Molecular Dynamics
N	Number of substances
V	Volume
E	Energy
P	Pressure
T	Temperature
H	Enthalpy
IK	Irwing-Kirkwood
LJ	Lennard-Jones
V_c	Unit Crystal Volume

CHAPTER 1

INTRODUCTION

Nanoscience and nanotechnology deal with an atomic or molecular level of substance. The atomic or molecular level is described as a substance with a size smaller than 100 nm. The idea of nanotechnology started with Richard Feynman in 1959[1]. Due to his inspiration, the manipulation of atoms and molecules is understood in many fields. Semiconductors, bioengineering, microfabrication, and chemistry are an example of these fields.

Due to the reduction of fossil fuels in the world and environmental problems caused by the consumption, optimization of energy consumption in all industrial applications has become extremely important. There have been great developments in electronics, communication, and computer technologies in the late twentieth century. These developments will likely continue in the following centuries. Along with all these developments, the size of the devices has shrunk.[2] However, the memory and operating rate of these devices increased. It led to heat transfer problems in these devices. Heat transfer studies have become more popular due to its high interest of society in devices since the 17th century. Firstly, researchers discovered the expression of Newton's cooling[3] law in 1701. After that in 1822, they discovered Fourier's law[4]. These formulations are used in two of three heat transfer methods which are conduction and convection. Although it was known that these heat transfer methods could break down small length scales such as micro and nanoscale, there was no need for this research at that time. Because of increasing electronic devices, research, and development activities in nanotechnology have become necessary in the last two decades.

The nanoscale heat transfer may be very different from what classical laws prescribe[5]. Understanding nanoscale heat transfer will assist to solve problems of thermal problems of devices that are used in daily life such as electronic devices. As mentioned before, research activities on nanoscale heat transfer have made a huge improvement over the last two decades, and many important phenomena have been discovered. Micro and nanoscale heat transfer are explored under the subject of the physical characteristics of transportation of energy which are electrons, phonons, photons, and the interaction

between these transport methods[6]. There are several fundamental reasons for heat transfer phenomena difference between macroscale and micro-and nanoscale. In macroscale, the heat transfer process is dominated by the internal thermal scattering in bulk materials[7]. However, the size of materials reduces in nanoscale. In this situation, the approach of transportation of heat is dominated by the interface dispersion of phonons and the related thermal boundary resistance[8]. Dispersion of the interface has a huge effect on the temperature-dependent thermal conductivities. Also, it has a big role in understanding thermal transport along with thin layers. Besides that, the effective way to remove heat from the devices is by changing phonon spectra[9].

One of the principal heat carriers in nanoscale heat transfer is phonons[10]. Understanding of physics of the phonons and their applications are the main study field in phonon engineering[11]. Phonon is vibrational due to the oscillation of atoms[12] in a crystal. The crystal is including highly ordered atoms, molecules, or ions called lattices[13]. Highly ordered structures create vibrations in lattices due to their thermal energy. These vibrations generate mechanical waves[14] that create heat transfer through the structure. These waves are moving in crystal with some energy and momentum and are called phonons. Phonon transport becomes an important phenomenon in nanoscale application areas such as nanoelectronics, optoelectronics, nanomechanics, and thermoelectrics.

One of the advanced technologies for data storage in hard disks that are used under the topic of heat transfer in nanoscale is heat-assisted magnetic recording[15], also known as HAMR technology. The main purpose is the increase the storage capacity. A diode with a laser attached is used to heating the recording section to reduce the coercivity of the magnetic field which comes from disk platter[16]. Each disk platter in the hard disk drive has grains[17]. More grains mean more data storage. To increase data storage, engineers placed the grains very close to each other to put more grain inside of the disk platter. However, this caused instability in the magnetic direction of the grains[15]. Also, thermal stability and heat dissipation problems occurred. To overcome these problems, HAMR technology is used in hard disk drives. The magnetic polarity of grains is changeable, and every grain is heated and cooled down in less than a nanosecond[18].

Researchers found a way to manipulate atoms and molecules to create different surface structures in nanoscale. The main purpose is to the investigate effect of surface patterns on surface wetting[19], heat transfer[20], etc. In this thesis, the effect of different surface structures on heat transfer is trying to be achieved. The cheapest and time-efficient

way to do this is using “Molecular Dynamics (MD)” method. MD[21] is a computer-based simulation to analyze the motion of atoms and molecules. MD simulations are very promising in the application of mathematical studies in many research and technological areas. The MD will be explained in detail in Chapter 3.

Another crucial topic is to understand the fundamentals and applications of heat transport in nanoscale is the transfer of heat in solid-liquid interfaces. MD simulations and experimental techniques are used in an investigation of the molecular-level of materials at solid-liquid interface[22]. This molecular-level thermal transport at the solid-liquid interface is represented by Kapitza length or Kapitza resistance. It is also called interfacial thermal resistance. Kapitza resistance is occurred due to a mismatch in the spectrum of phonon and discovered by Kapitza in 1941[23]. This term is also will be explained in detail in Chapter 2.

CHAPTER 2

FUNDAMENTAL CONCEPTS AND RELEVANT LITERATURE

2.1. Heat Transfer in Nanoscale and Current Applications

Heat transfer is the physical action of thermal energy exchanged by dissipating heat between two systems. Temperature and heat flow are the major factors of heat transfer[7]. Temperature is used to determine the amount of thermal energy available, and heat flow indicates the movement of thermal energy. Nanoscale heat transfer is important for many nanotechnology applications. There are two major problems. One of them is the manipulation of heat dissipation[9] in nanoscale devices to maintain functionality and reliability. The other one is to use nano-scale structures to utilize heat flow and energy conversion[24]. Heating problems in integrated circuits[25] and semiconductor lasers[25] are examples of manipulation of heat dissipation. Data storage[26] and thermoelectric energy conversion[27] are examples of heat flow and energy conversion.

One of the important fundamentals in device integration is Moore's law[28]. Moore's law is stated by Gorden Earle Moore who is co-founder of Intel. He stated that "The number of transistors incorporated in a chip will approximately double every 24 months". However, according to today's technology, number of transistors incorporated in a chip will approximately double every 18 months. In other words, the current situation went beyond Moore's law. In 2020, the total number of transistors in CPU and GPU systems is around 10^{10}. Also, the size of the transistors[29] has become 14 nm, 12 nm, 10 nm, and 7 nm. As the size decreases, the density which is transistor per area increases. Figure 2.1a and 2.1b show the changing number of transistors and size of the transistors in CPU and GPU, respectively, by years. Also, Figure 2.1c shows the changing density with respect to transistor size.

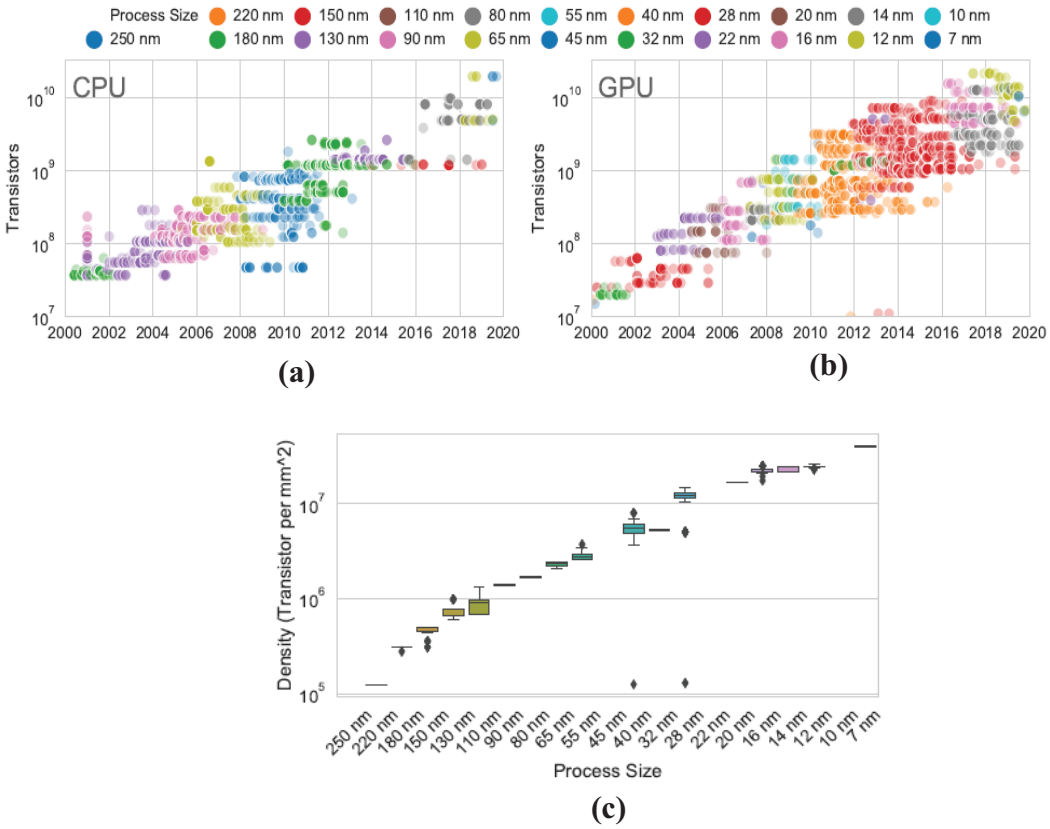

Figure 2.1. (a) Changing number of transistors and transistor size in CPU by years[29]. (b) Changing number of transistors and transistor size in GPU by years[29]. (c) Changing density with respect to transistor size[29].

The reduction of transistor size increased the computing capabilities of the devices. Also, it increased the die density (number of transistors per area). However, it led to heat dissipation problems in these devices. As a fact that, if the trend of increase in the number of transistors in CPU or other devices continues according to Moore's law, the total heat flux of these devices will eventually reach the heat flux of the surface of the sun[30]. The future trend is the transition from single-core architecture to multi-core architecture to prevent the amount of heat dissipation.

Heat transfer at macro-scale and nanoscale are two very different fields of study. In nanoscale, the characteristic length of the device must be analogous to the wavelength of electrons, phonons, and molecules[6]. In this condition, classical laws of heat transfer may not be enough[5], and new methods have to be used to characterize heat transfer at nanoscale. Although many studies have been done in this area recently, there is an urgent need for a better understanding of the transfer of heat in nano-sized designs.

Energy generation and transport is an important process in a wide range of engineering applications. Nanoscale heat transfer which is discussed in this chapter is used in many modern technologies from microelectronics to bioengineering[9]. There are plenty of areas that nanoscale heat transfer is used. One of them is in information technologies. Nanoscale heat transfer phenomena are widely used in information technologies under the topic of microelectronics, and data storage devices which are hard-disk[6]. Because heat dissipation of microelectronics and hard-disk drives creates considerable issues. As an example, FinFET[31] (Fin field-effect transistor) is a type of non-planar transistor. It is the invention that forms the basis of modern nanoelectronic semiconductor device fabrication. Figure 2.1 represents the indication of the size of a transistor in the early years and predicts the thermal conductivity of silicon material which has a relation with the size of the transistor. FinFET designs improve the node of the transistor from 800 nm node to 14 nm node[32]. SiC[31] and diamond[31] are materials that are used in this type of design to improve heat dissipation and minimize interfacial thermal resistance.

Another area that nanoscale heat transfer used is energy conversion. Thermoelectric cooling[33] and power generation[34] are examples of energy conversion. Nanomaterial synthesis[35] and nanofabrication[36] is another area that nanoscale heat transfer is used. To manufacture cheap electronics, nanocrystals that have a size-dependent melting point may be used. Nanoscale heat transfer has also made progress in biotechnology[37]. To control DNA hybridization[38], inductively heating gold nanoparticles are attached to DNA strands.

2.2. Kapitza Length

2.2.1. Definition of Kapitza Length

Transfer of heat at solid-liquid interfaces is one of the most important studies in nanoscale and microscale. In nanoengineering[39], understanding the microscopic characteristics of nanoscale devices is a crucial phenomenon. Transfer of thermal energy at the solid-liquid interface is one of the molecular scale phenomena and to investigate it, both experimental and computational studies are used.

Characterization of transportation of thermal energy at the solid-liquid interface is done by using Kapitza Length or Kapitza Resistance[23]. Kapitza resistance is also called thermal boundary resistance or interfacial thermal resistance in literature and it is an important term in nanoscale systems. Kapitza length is discovered by Kapitza in 1941[23]. Kapitza used helium as a superfluid[40]. Then, he found a strong thermal resistance when helium and solid surface contact. Later, Khalatnikov[41] created a model that includes interfacial thermal resistance in all temperature ranges. As mentioned in section 2.1, he found that the confined fluids at nanoscale may break the most known macroscale theories such as Navier-Stokes equations[42] and no-slip boundary condition[43].

Kapitza resistance is occurred due to a mismatch in a spectrum of phonon. When energy is transferred through a system, a temperature jump occurs at the solid-liquid interface due to thermal velocity difference[44]. Because of the velocity difference, particles create different momentums at the solid-liquid interface[44]. This momentum difference is directly related to the kinetic energy of the system. In weak molecular interactions, temperature jumps are observed due to sudden changes in kinetic energy. However, in strong molecular interactions, there is no temperature jump observed.

Kapitza length can be calculated as below:

$$\Delta T = L_K \left.\frac{\partial T}{\partial n}\right|_{liquid}, \tag{2.1}$$

where temperature jump is $\Delta T = t_{fluid} - t_{wall}$, and $\partial T/\partial n$ is the temperature gradient. For nano-confined liquid, interfacial heat transport phenomena of temperature jump can be calculated directly by using temperature profiles from analytical solutions. This phenomenon is proven experimentally and increase the attention of the nanofluidics field. As an alternative to experimental methods, molecular dynamic simulations have been used as a powerful tool for investigating Kapitza length. Because MD simulations are one of the cheapest and time-efficient ways to utilize these kinds of studies.[45]. Representation of Kapitza length and the temperature jump can be seen in Figure 2.2.

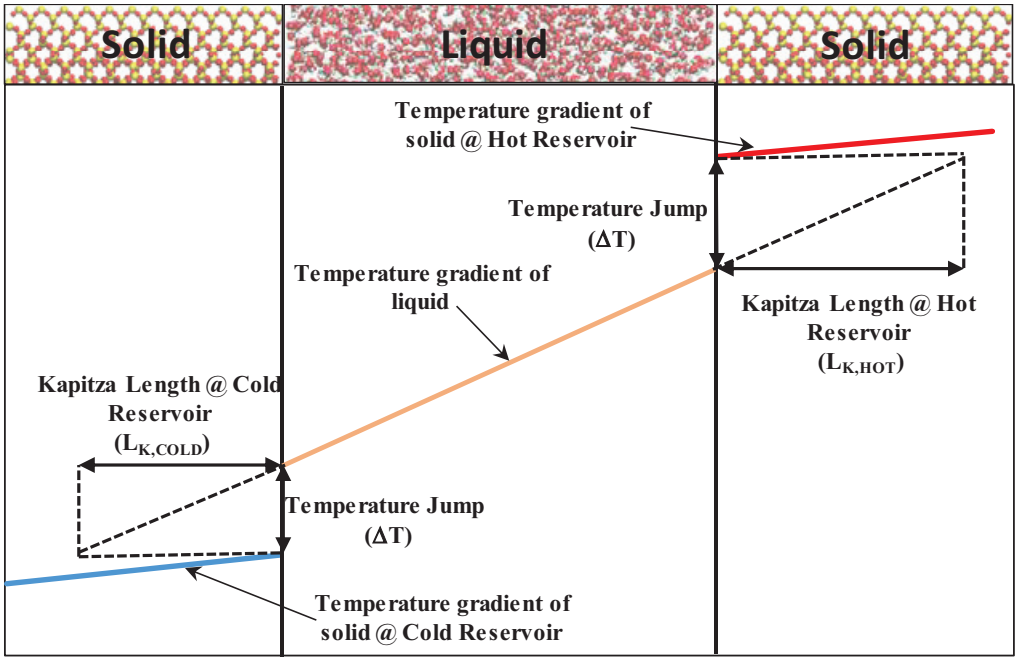

Figure 2.2. Representation of Kapitza length (L_K) and the temperature jump (ΔT) at liquid-solid interface.

2.2.2. Kapitza Length Studies in Relevant Literature

There are several ways to predict Kapitza length in the literature. Researchers used two different approaches to utilize heat transfer in solid-liquid interfaces. These are Acoustic Mismatch Model[46] (AMM) and Diffusion Mismatch Model[47] (DMM). In Acoustic Mismatch Model, heat is transferred between solids using elastic waves. These elastic waves create temperature jumps[48]. However, the Diffusion Mismatch Model is based on the theory that energy is transferred by quanta of elastic waves, phonons, and quasi-particles. Additionally, AMM is considerable for high interfacial thermal resistance, while DMM is considerable for low interfacial thermal resistance[48]. In the literature, Khvesyuk et al.[49] investigated Kapitza length for metal-sapphire and metal-silicon interfaces by using AMM and DMM methods. They calculated Kapitza length values for metal-silicon and metal-sapphire interfaces. Metals which are aluminum, copper, indium, lead, tungsten, chromium, magnesium, nickel, platinum, rhodium, and silver are used in their study. However, these methods are old fashioned and expensive.

Besides that, detailed information of elements or molecules cannot be predicted by using these two methods.

To predict detailed information of nanoscale structures, Molecular Dynamics Simulation is frequently used. Using the MD method will help to obtain properties such as a chemical bond, and geometry[50]. This method is quite effective and cheap. In the literature, there are several studies of investigation of Kapitza length by using the Molecular Dynamics method. Most of the studies include two parallel solid walls and between them, there is a layer of liquid molecules.

Most of the simulation techniques include a solid-liquid interface to obtain Kapitza length. Different solid and liquid molecules are used to investigate the interfacial thermal resistance or Kapitza length. Kapitza length has a relation with different parameters such as weak or strong interaction between solid and molecules, the initial temperature difference of the system, liquid/solid density, surface wettability, channel height, thermal gradient, wall temperature, oscillation frequency, and solid thickness.

To investigate the effect of interactions between solid and liquid molecules on Kapitza length, Pham et al.[51] used 3D MD simulation using argon-silicon and water-silicon interfaces. The model is basically including two parallel solid walls and between the walls, there are water and argon molecules. NEMD is used to investigate heat transfer by applying thermostats. They also observed temperature jumps which lead to Kapitza length at silicon-water and silicon-argon interfaces. To calculate Kapitza length at the solid-liquid interface, they plotted temperature profiles of silicon-water and silicon-argon model, and equation 2.1 is used. The temperature gradient of the solid region is less than the liquid region due to its thermal conductivity. When finding Kapitza length for two different models, they set hot and cold reservoir temperature 323 K and 283 K, respectively. Then, they increased 10 K of each wall temperature to increase the temperature of the system. At the same time, they kept the temperature difference constant. The cold region has 283 K while the hot region has 363 K. After the calculations, they found that Kapitza length has no relation with the temperature of the wall for two different models. The values have fluctuated around an average value between 283 K and 363 K. They also found that Kapitza length is higher on weak solid-liquid interaction. Kapitza length which is calculated at the silicon-argon model is one-third of the silicon-water model because of the thermodynamics properties of water[51]. Kim and Beskok[52] also studied the effect of molecular interaction on Kapitza length at a solid-liquid interface.

They created a molecular dynamics simulation that can simulate the heat transfer in a nano-sized structure using a new model of walls. The new model creates interaction between fluid molecules. According to the temperature distribution plot, they observed sudden changes in temperature at the interface. The results show that there are not any temperature jumps in strong molecular interaction. However, there are temperature jumps in weak molecular interaction. The reasons for the temperature jumps are weaker interactions and crystal bonding stiffness. They also found that the temperature distribution near the interface can be affected by bonding stiffness of the crystal.

Later that, researchers investigated the effect of both surface wettability and solid/liquid density at the same time on Kapitza length. Firstly, Barisik and Beskok[53] investigated the thermal transport of a water-silicon system to obtain thermal resistance at a water-silicon interface by using MD simulations. To observe the effects of water and silicon, interaction strength is decided. They developed different distribution of water molecules to investigate wetting behavior. Then, they computed Kapitza length values of the interface and found that it has a direct relation with different forms of water density. Barisik and Beskok performed a density distribution of a water-silicon system for different ε_{Si-O} values. Silicon and water density are observed as 2.35 g/cm^3 and 1.006 g/cm^3 respectively. The temperature of the hot reservoir and cold reservoir were kept as 353 K and 293 K respectively. They found that the layer of the water molecules become stronger when the molecular interaction strength parameter increased. They also characterized a temperature profile for three different temperature difference for a condition of $\varepsilon_{Si-O}/\varepsilon^*_{Si-O}$=0.125. 363, 353, and 343 K are the temperatures of the hot reservoir while the temperatures of the cold reservoir are 283, 293, and 303 K. Later that, they calculated Kapitza length for a cold and hot reservoir. Kapitza length values are measured around 9 nm for using MD simulations which are matched with experimental results for $\varepsilon_{Si-O}/\varepsilon^*_{Si-O}$=0.125 condition. Yenigun and Barisik also investigated the effect of surface wetting on Kapitza length with different thicknesses of silicon walls. The results showed that when surface wetting is changing from hydrophobic to hydrophilic, Kapitza length decreases. However, the variation of slab thickness showed a universal behavior. The effect of slab thickness on Kapitza length will be explained in future paragraphs.

The effect of oscillation frequency on Kapitza length is also studied in the literature. Kim and Beskok[52] created an MD simulation between two parallel solid plates

and between them there are liquid Argon molecules. They calculated heat flux and temperature distribution by changing the height of the channel which varies between 12.96 nm and 3.24 nm. They also observed temperature jumps at the interface. In this study, Kapitza length is characterized as a function of oscillation frequency, wall temperature, thermal gradient, and channel height. The result showed that Kapitza length increased when thermal oscillation frequency increased. Also, Kapitza length increased when wetting of the surface decreased.

Another parameter that can affect Kapitza length is the temperature gradient and initial temperature difference of the simulation. To observe effects, Balasubramanian et al.[50] investigated heat transfer at the solid-liquid interface by using MD simulations. They used iron (Fe) walls and liquid argon is placed between the walls. The main purpose is to observe the temperature gradient in the system. They observed quasi-crystalline layers. The reason for this is the interaction between iron and argon. This causes sudden temperature jumps between solid-liquid interface. They observed Kapitza length and Kapitza resistance has a relation with temperature difference parameters of wall and fluid and this relation can be expressed as equation (2.2).

$$R_{k,av} = (3x10^{-6})\Delta T_w{}^{-0.82} \tag{2.2}$$

As mentioned in previous chapters, there have been great developments in electronics, communication, and computer system. Depending on developments, component sizes that are used in these systems have been decreasing to nanometer scales. The decreasing size of the devices creates a new field of study for researchers. According to the literature, Kapitza length can be affected by changing the thickness, width to space ratio, depth, and height of the nanopattern. To see the effect of thickness of the nanopattern on Kapitza length, Yenigun and Barisik[54] developed a water-silicon system by using MD simulations. This system has thickness parameters that vary between 5 nm and 60 nm. As a result, thermal conductivity increased when silicon wall thickness increased. However, Kapitza length decreased at the same condition.

Later, the relation between velocity slip and temperature jump has become a curious topic among researchers. Unfortunately, there have been very few studies for creating a model that including the relation between temperature jump and velocity slip in the relevant literature. Velocity slip and temperature jump are quantified by “Slip

Length (L_s)" and "Kapitza length (L_K)" on solid-liquid bonding, respectively. In recently, researchers tried to find a relation between L_s and L_K. Kalyoncu and Barisik[55] found L_s and L_K values from literature with the same surface and flow conditions. They tabulated the measured L_s ranges and L_K ranges together which is shown in Table 2.1.

Table 2.1. Measured slip length ranges and Kapitza length ranges from relevant literature.[55]

Study	**L_s (nm)**	**L_K (nm)**	**L_K=k x L_s**	**k**
Kou and Bai	0.4-2.2	1.84-11.35	$L_K=3.03L_s$	3.03
Sun et al.	5.29-8.52	0.49-17.14	$L_K=4.87L_s$	4.87
Sun et al.	1.64-4.55	1.89-22.24	$L_K=7.13L_s$	7.13
Thekkethala and Sathian	17.7-28.78	0.06-6.90	$L_K=0.61L_s$	0.61

Roy et al.[56] found that the ratio of slip length to Kapitza length is equal to Prandtl number (Pr) for gas flows. A similar approach is used by Kalyoncu and Barisik for liquid flows. However, the linear relationship of L_s and L_K is more complex in liquid forms since the momentum and heat transfer approach is much difficult than gas forms. They used the values from Table-1 and calculated k parameters for the $L_K=kxL_s$ relationship. As mentioned in Table-1, Sun et al.[57] found an approach between velocity slip and temperature jump on solid bonding. They identified two different regimes which are weak and strong to investigate the interfacial parameters of nano liquid. They found that Kapitza length is changing with slip length and interaction parameter and found a relation which is shown in equation (2.3). However, Kapitza length was stable in the strong regime.

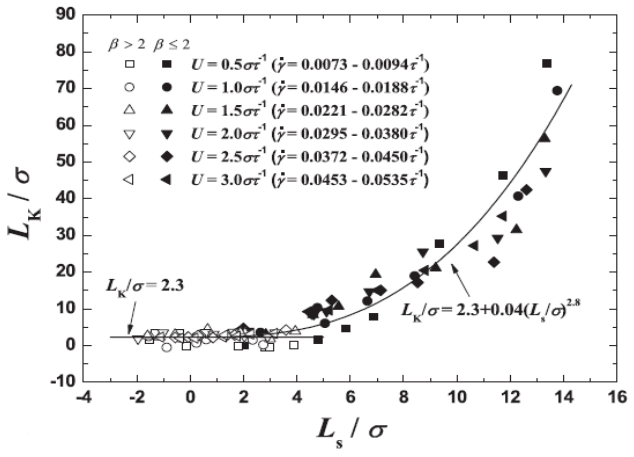

Figure 2.3. Kapitza length (L_K) vs slip length (L_S)[57]

Figure 2.8 shows the relation between L_K and L_s according to studies of Sun et al. They called weak solid-liquid interaction regime as $\beta \leq 2$, and strong solid-liquid interaction regime as $\beta > 2$. They expressed two equations for two conditions:

$$\frac{L_K}{\sigma} = 2.3 + 0.04\left(\frac{L_s}{\sigma}\right)^{2.8}, \qquad \text{for } (\beta \leq 2) \tag{2.3}$$

$$\frac{L_K}{\sigma} = 2.3, \qquad \text{for } (\beta > 2) \tag{2.4}$$

2.3. Effects of Surface Pattern and Surface Roughness on Kapitza Length

In section 2.2, effects on different parameters on Kapitza length are explained using literature studies. However, relation to the manipulation of surface patterns and related roughness parameters and Kapitza length is main purpose of this thesis. Different studies are approached in the literature about this relation. To investigate the effect of depth of the cavity or called nanogroove depth on interfacial thermal resistance at the graphene-copper interface, Hong et al.[58] performed MD simulations using LAMMPS open-source. To obtain a stable simulation, graphene nanoribbon (GNR) is used. In the simulation domain, two different forms of nanobumps are cylindrical and rectangular. Cylindrical and rectangular nanobumps have 0.83 nm nanogroove depth and 2 nm nanogroove width. Note that, changing of Kapitza resistance with different nanogroove depth also observed. The interfacial thermal resistance of the smooth pattern is calculated as 2.61 x 10^{-8} Km^2W^{-1}. By using different nanogroove depth dimensions, Kapitza resistances reduced 17% at 2 nm width and 0.63 nm depth[58]. Also, Kapitza resistance values decreased in cylindrical nanobumps compared to rectangular nanobumps. The reason for the decrease is that supported regions have high local pressures.

To investigate the effects of smooth and rough surface patterns on Kapitza length, Wang and Keblinski[59] created a non-equilibrium molecular dynamics simulation using a metal-liquid helium interface. They studied temperature profiles of smooth and rough patterns to approach Kapitza length. The temperature drops of the rough surface are much higher than the smooth surface. The reason is the reduction of the solid-liquid interface area. The interfacial thermal conductance or Kapitza conductance (G_K) is determined by using heat flux which is applied to interface and temperature drop. On the smooth surface,

Kapitza conductance increased monotonically when the roughness of the surface increased. However, on the rough surface, Kapitza conductance made a sharp increase at some critical point, then increased[59]. Then, a similar study with the different surface patterns is approached by Zhou et al.[60] by using large direct-method MD simulations. Al-Ga-N molecular relationship with EAM method is used to investigate Kapitza conductance with the surface pattern which has different interfacial roughness parameters. First, they created a model that has the same cross-section and cavity width but different cavity depth. These cavity depths are 0 Å, 10 Å, and 34 Å, respectively, and represented as δ. Figure 2.4 (a) shows the simulation model of their study. After the model is created with different depths, temperature profiles are obtained. Using the temperature profile data, Kapitza conductance for different cavity depths is calculated and shown in Figure 2.4 (b).

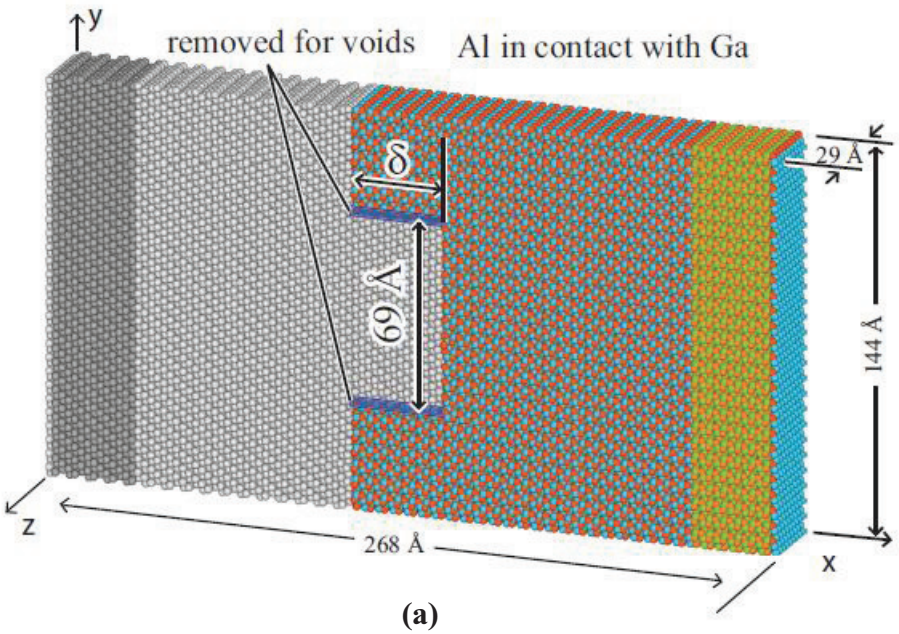

(a)

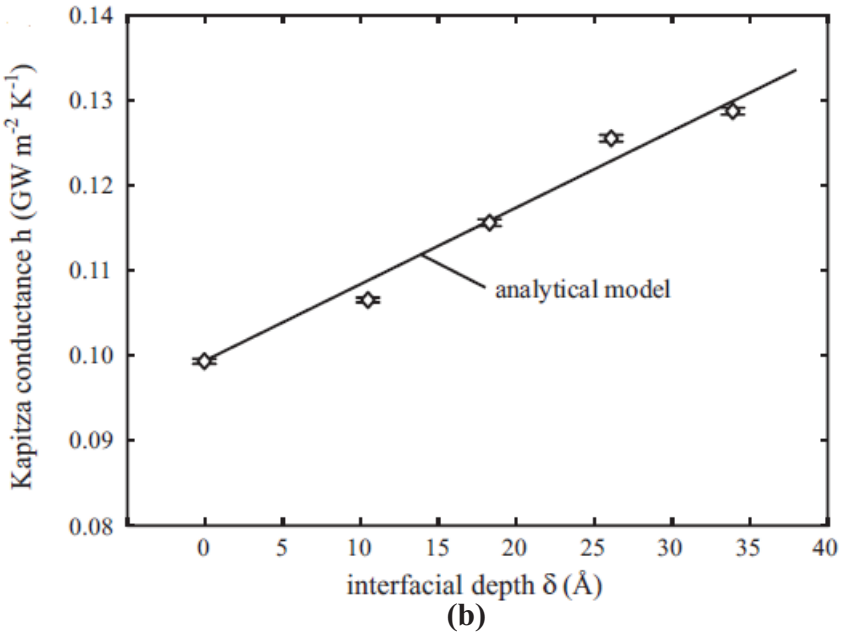

Figure 2.4. (a) Snapshot of the model.[60] (b) Relation between Kapitza conductance and cavity depth.[60]

When cavity depth increased, the length between the two interfaces is increased. This causes different sudden temperature drops at the interface. However, when cavity depth decreased to 0 Å, also called smooth pattern, the left, and right interfaces overlap and created only one temperature drop at the interface. To investigate clearly, Kapitza conductance is computed for different interfacial depth. Results showed that Kapitza conductance increased when interfacial depth increased. The smooth pattern has the lowest Kapitza conductance which is δ=0 Å. After that, they investigated Kapitza conductance by using different surface geometries such as sinoidal, triangular, and rectangular. They fixed cavity width as 36 Å and cavity depth as 10 Å. Figure 2.5 shows the simulation model with different surface geometries. The Kapitza conductance values are computed as 0.157, 0.176, and 0.196 GW m^{-2} K^{-1} for triangular, sinoidal, and rectangular geometries, respectively. Triangular geometry has the smallest cross-sectional area while rectangular geometry has the biggest cross-sectional area. The results showed that the rectangular geometry created greater Kapitza conductance than sinoidal and triangular geometry. Also, Kapitza conductance of sinoidal geometry is greater than triangular geometry.[60]

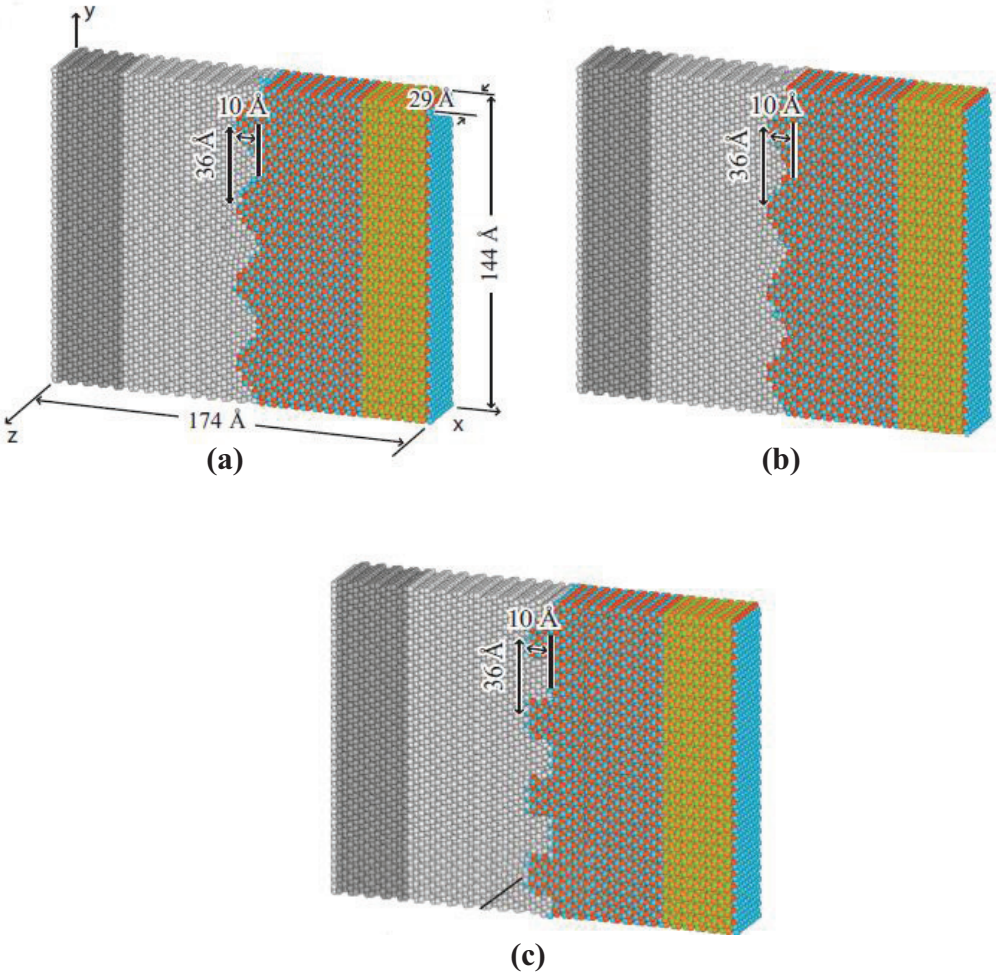

Figure 2.5. (a) Sinoidal geomethry.[60] (b) Triangular geomethry.[60] (c) Rectangular geomethry.[60]

Up to this point, the temperature jumps at the interface are characterized as Kapitza resistance and Kapitza conductance, respectively. However, there are also studies which are covering Kapitza length. Sun et al.[61] studied the roughness effect on thermal boundaries using continuum hybrid molecular dynamic simulations. Changing Kapitza length with respect to channel height is observed. Continuum hybrid MD simulations have 3 different regions. These are particle region (P), continuum region (C), and overlap region (O). Temperature jumps for rough conditions are constant while channel height increased. However, temperature jumps are decreased in smooth conditions compared to rough conditions. In smooth conditions, Kapitza length remains constant while channel height increased. However, Kapitza length is increased while channel height increased in rough conditions. Three different roughness parameters which are h=0, h=3.32σ and h=6.64σ are used to observe the changing of Kapitza length. Results showed that both

absolute and relative Kapitza length of rough surfaces are higher than the smooth surface. Also, Kapitza length of the h=3.32σ condition is higher than h=6.64σ. This proves that there are critical roughness and channel height parameters to obtain the highest Kapitza length value.[61] After that, Sun et al.[62] improved the study by changing the surface geometry of continuum-hybrid MD simulation to investigate effects of channel height (H), roughening dimensions which are height (h), length (w), and pitch (p) in the x-direction, and liquid-solid bonding factor (β) on Kapitza length. After continuum-hybrid MD simulations are solved, effects of channel height (H), (p/w) ratio and β on relative Kapitza length are observed. The results showed that relative Kapitza length (L_K/H) has very similar behavior in different conditions. Relative Kapitza length has a sharp decrease in small channel heights while it has a slight decrease in bigger channel heights. Also, L_K/H increased while (p/w) ratio increased. But the increment rate decreased. Finally, L_K/H has a sharp decrease in small liquid-solid bonding factor while it has a slight increase in greater liquid-solid bonding factor.[62] All the results of relations of different surface geometries with relative Kapitza length are shown in Figure 2.6a, 2.6b, and 2.6c.

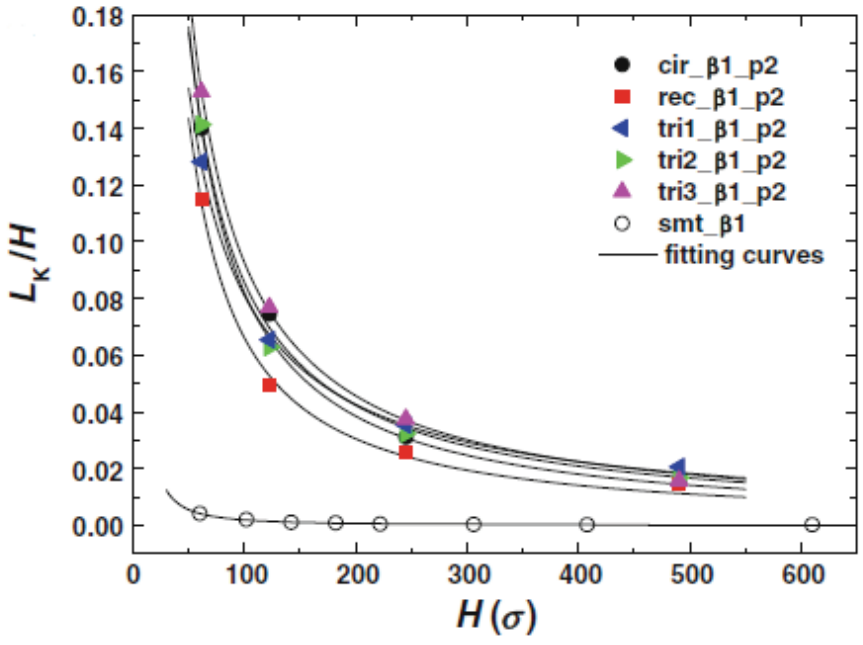

(a)

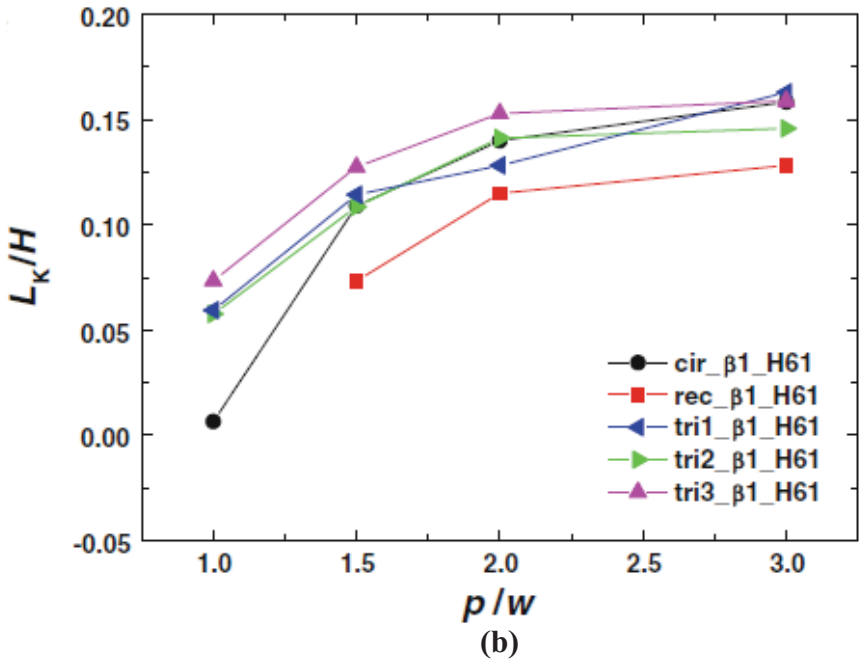

(b)

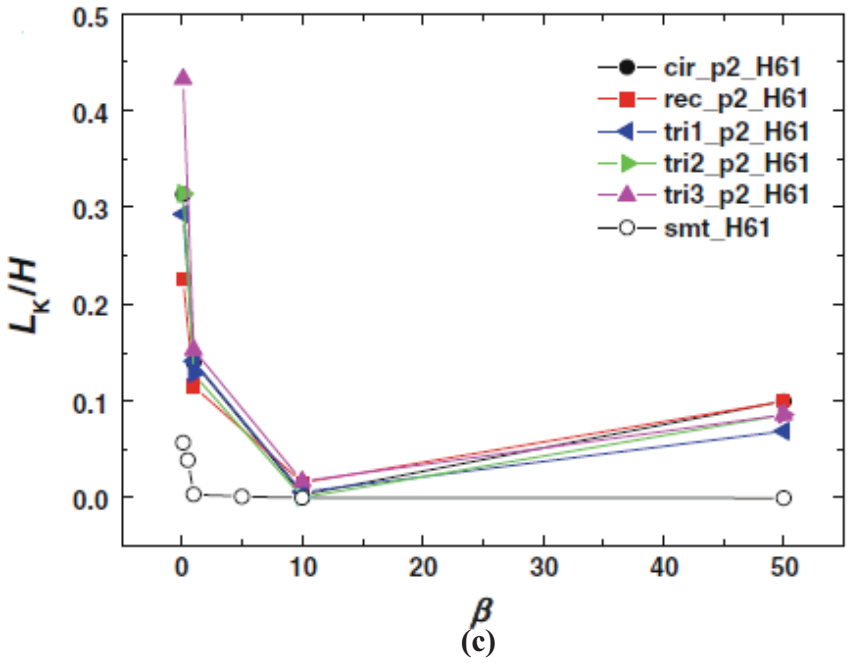

(c)

Figure 2.6. Changing of relative Kapitza length[62] with respect to (a) Channel height, (b) (p/w) ratio, (c) Solid-liquid bonding factor.

CHAPTER 3

THEORETICAL BACKGROUND

3.1. Molecular Dynamic Approach in Nanoscale

Molecular Dynamics is a promising method to investigate heat transfer at the nanoscale. MD works directly with using the molecular level of substance. To obtain a nanoscopic system, MD solves Newton's equation of motion and applies this to every molecule in the simulation domain. The history of MD simulation starts between the 1950s and 1960s. In 1957, Alder and Wainwright[63] investigated particle dynamics. After that, in 1964, Rahman[64] found a way to apply Newton's equation of motion to LJ particles. In MD simulations all interconnected parameters must be computed to obtain a reliable simulation domain. Also, the needed potentials should be computed and solved by using quantum mechanical calculations. However, these calculations are difficult to approach.

In molecular dynamics, the first step is the represent every atom and its exact position in the system. After that, the system domain is initiated by applying periodic boundary conditions. Next, potential functions are used to obtain interatomic interactions. The final step is applying ensembles and time integration.

3.1.1. The Fundamentals of Molecular Dynamics

The main fundamental of MD simulation is the determination of the basic dynamic parameters of every atom or molecule such as position, velocity, and interaction forces. Then, macroscopic physical properties such as pressure, temperature, and volume must be obtained by using statistical methods. According to these approaches, the origin of MD simulations is Newton's second law which all existing forces are balanced[65]. The simple form of Newton's second law:

$$F = m\frac{d^2r}{dt^2}, \tag{3.1}$$

where F is the net force exerted on the molecule, m is the mass of a molecule, r is the

position vector of the molecule, and t is the time. Integrating equation 3.1 once with respect to time gives the velocity and integrating twice gives the displacement. To obtain further information about the movement of each molecule in the system, the velocity profile equation must be solved step by step by using some initial state. Using time and space averaging methods[64] helps to improve the equation of velocity profile and. However, some molecules in the simulation may have an internal complex geometry. In this condition, Newton's second law cannot be used. Generalized Newton's equation can be used. The simulation procedure always the same regardless of the complexity of Newton's second law[65] (also known as the equation of motion). First, integrate once or twice to the equation of motion to obtain dynamical parameters of the molecule. Then, apply averaging methods to dynamical parameters. In the end, the physical properties can be achieved.

As mentioned before MD deals with classical forces and the calculation of these forces is relatively difficult. Because normally these forces are electric or electromagnetic[66]. To get the right solution, these forces should be determined correctly in the intermolecular potential model. Using two or three body potentials[63], quantum mechanics, and experimental data which came from the original model help to overcome this problem. If a two-body potential method is applied, the force equation derived as:

$$F_{ij} = -\nabla u_{ij}, \tag{3.2}$$

where F_{ij} is the force exerted on the molecule and u_{ij} is the two-body potential. To get total force, all forces exerted on a molecule by another molecule should be summed. When the total force is calculated, Newton's equation of motion can be integrated with respect to time for each molecule in the system[67].

The most popular potential in MD simulation is Lennard-Jones (LJ) potential. Lennard Jones[68] potential assumes that all the molecules in the system are spherical. According to this assumption LJ potential can be derived as:

$$u(r) = 4\varepsilon\left[\left\{\left(\frac{\sigma}{r}\right)^{12} - \left(\frac{\sigma}{r}\right)^{6}\right\}\right], \tag{3.3}$$

where σ is length scale, ε is the energy scale, and r is the intermolecular distance. These terms are shown in Figure 3.1.

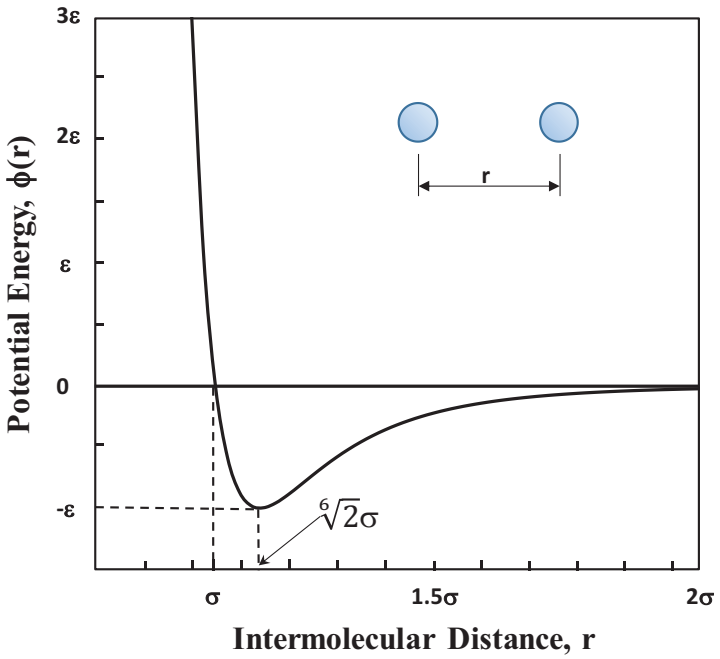

Figure 3.1. Lennard Jones potential[21]

Equation 2.7 explains that energy must be removed to bring two molecules to a closer distance. In other words, if two molecules are at a close distance from each other they can feel attractive forces. However, this distance may not be enough to feel repulsive forces. In this condition, energy should be provided to increase the r.

3.1.2. Molecular Dynamics Approach in Nanoscale Heat Transfer

Investigation of the molecular level approach is becoming a major subject to understand heat and mass transfer in micro or nanotechnologies. As an example, phase change[69] is the one of the bases of heat transfer. To understand phase change in nanoscale, liquid-solid contact should be learned. MD simulations have been used statistically for a long time in the fields of mechanics and chemistry. However, heat transfer phenomena are a new research area for MD simulations. Some macroscopic parameters are used to define the system at the macroscale. However, on the microscale, these parameters must be converted to the nanoscale. The challenge is the conversion of these parameters.

Phase change process and heat conduction are the two areas that are used in heat transfer in nanotechnology.

3.1.3. Potential Functions

The most fundamental potential function in MD simulations is Lennard-Jones potential. Lennard Jones is explained in Section 3.1.1 and represented in Figure 3.1. The other one is the van der Waals[70] interaction. Van der Waals interaction is usually approached by using Lennard Jones potential. This interaction is mostly described in electrostatic origin and depending on the dielectric properties of the environment. Van der Waals interaction is modeled using truncated 12-6 Lennard Jones potential and can be given as:

$$\phi_{truncated}(r_{ij}) = 4\varepsilon\left[\left\{\left(\frac{\sigma}{r_{ij}}\right)^{12} - \left(\frac{\sigma}{r_{ij}}\right)^{6}\right\} - \left\{\left(\frac{\sigma}{r_c}\right)^{12} - \left(\frac{\sigma}{r_c}\right)^{6}\right\}\right], \tag{3.4}$$

where r_{ij} is the intermolecular distance, ε is the depth of the potential, σ is the molecular diameter and r_c is the cut-off radius. Another potential that is used in molecular dynamics simulations is the Coulombic potentials[71]. Electrostatic interaction between two atoms is described by using Coulombic potential and can be given as:

$$\phi_{Coulombic}(r_{ij}) = \frac{Cq_iq_j}{4\pi\varepsilon_0 r_{ij}}, \tag{3.5}$$

where ε_0 is the vacuum permittivity, q_i and q_j are the partial charges, r_{ij} is the distance between two charged atoms. Also, $C/4\pi\varepsilon_0$ is known as the Coulomb force constant.

Lennard-Jones potential is the most common method for a similar type of atoms, but a dissimilar type of atoms is also used in this thesis. To calculate the interactions between dissimilar atoms, Lorentz-Berhelot[72] combining rules are applied and these equations can be given by using silicon-oxygen interaction as an example:

$$\sigma_{Si-O} = \frac{\sigma_{Si-Si}+\sigma_{O-O}}{2} \tag{3.6}$$

$$\varepsilon_{Si-O} = \sqrt{\varepsilon_{Si-Si}x\ \varepsilon_{O-O}} \tag{3.7}$$

Also, heat flux must be considered for the continuum mechanics model. Irving-Kirkwood[73] (IK) is developed a continuum mechanics model and this model can be expressed as conservation of mass, momentum, and energy. Both Eulerian and Lagrangian coordinates are used to define this expression. The lagrangian coordinate of

Irving-Kirkwood expression for heat flux vector calculation in the system can be given as:

$$J_k = \frac{1}{Vol}\left[\sum_i^N V_k^i \left(E^i + \phi^i\right) + \sum_{i,j}^N \left(r_k^j + r_k^i\right) W^{i,j}\right], \quad (3.8)$$

$$E^i = \frac{1}{2} m^i \left[\left(V_x^i\right)^2 + \left(V_y^i\right)^2 \left(V_z^i\right)^2\right], \quad (3.9)$$

$$W^{i,j} = \frac{1}{2}\left(V_x^i f_x^{i,j} + V_y^i f_y^{i,j} V_z^i f_z^{i,j}\right), \quad (3.10)$$

where, V_k^i is the peculiar velocity component of particle i in k-direction, E^i (equation 3.8) and Φ^i are the kinetic and potential energies of the particle i, ($r_k^j + r_k^i$) is the k^{th} component of the relative distance vector between particles i and j, $W^{i,j}$ term is given in Equation 3.10, where $f_l^{i,j}$ is the intermolecular force exerted on particle i by particle j in the Cartesian coordinate direction l. First-term on the right-hand side of equation 3.8 describes the kinetic and potential energies carried by the particle i, while the second term represents the energy transfer by force interactions with the surrounding particles to particle i. By considering the contributions of each atom within a water molecule, overall heat flux is calculated in the water volume using equation 3.8.

3.2. Modelling of Water

Water is a complex molecule because of its thermodynamic properties. Because of this complexity, different water models are used in molecular dynamics. Depending on the application in the simulation, a specific water type should be modeled. Several water types are used in MD simulations in the literature. These are TIP3P[74] (Transferrable Intermolecular Potential 3-Point), TIP4P[74] (Transferrable Intermolecular Potential 4-Point), SPC[75] (Simple Point Charge), and SPC/E[75] (Simple Point Charge Extended). Besides that, SPC/RF[76] (Simple Point Charge Reaction Field), and TIP4P/RF[76] (Transferrable Intermolecular Potential 4-Point Reaction Field) are used rarely in the literature. To obtain thermodynamically and electrostatically stable water models, Lennard-Jones potential, and Coulombic potential are used. When modelling water, the bond angle between H and O atoms and bond length is specified. After the specification of these terms, suitable water type and algorithm should be applied. Different types of algorithms are used in molecular dynamics simulations for water modelling. These are

SETTLE[77], M-SHAKE[78], SHAKE[79], SHAPE[80], and LINCS[81]. According to the properties of the system, the algorithm choice may be different.

3.3. Selection of Silica

Silica is one of the most common substances on Earth and its chemical formula is SiO_2. Approximately 58% of the lithosphere is made up of bonded SiO_2 and 12% of this silica is discovered in the form of quartz, chalcedony, and opal[82]. Silica is a unique material due to its wide-range of modifications and is used in many technological areas. The reason for this is the physical, chemical, and thermal properties of silica. Silica has high-temperature stability up to 1600° C and this makes it an important material for device integration. Silica is used as an insulator due to its electrical properties. Also, it is resistant to many chemicals. Silica is a main component of glass, optical fibers. It is also used in microelectronics as a thermal and electrical insulator and diffusion barrier[83].

Silica or called silicon dioxide is a unique substance due to its bonding anatomy. For example, carbon has a maximum of four coordination number. However, silicon has up to five or even six coordination number. Tetrahedral angle[83] of Si-O-Si is considered as 109.28°. However, depends on the structure of silica, this angle can vary in the range between 120° and 180°.

Due to advances in high-pressure techniques, two common silica forms are created. These are crystalline and amorphous. Also, SiO_2 has many different detailed forms and mainly derived quartz glass. These are beta-cristobalite[84], beta-quartz[85], alpha-quartz[85], beta-tridymite[86], alpha-tridymite[86], alpha-cristobalite[84]. These silica structures have the same chemical composition but different crystal structures. Because of this, they are called polymorphs.

As mentioned before, quartz is the most general form of silica. It has two polymorphs: alpha-quartz or called low-quartz, and beta-quartz or high-quartz. The structures of alpha and beta quartz are built from helical arrangements of SiO_4 tetrahedra.[87] Also, quartz has a non-symmetric structure due to its piezoelectricity[88] property. It means that when quartz is deformed, it creates electric potential. Because of this property quartz is the main material of oscillators, quartz watches, etc. The other polymorphs of silica are tridymite and cristobalite. Tridymite has a hexagonal crystal system while cristobalite has a cubic crystal system. The difference between alpha and

beta forms of tridymite and cristobalite is that alpha forms are discomposed forms of beta forms with lower symmetry and lower temperatures. In other words, beta forms of silica polymorphs have higher temperatures and good symmetric structure while alpha forms have lower temperatures and lower symmetry. Changing polymorphs alpha to the beta is came from laws of thermodynamics. Changing the physical property and then giving some kinetics will help to change one silica polymorph to another. Since there is bond breaking in this process, it is called reconstructive transformation[89].

Beta-cristobalite was used as a polymorph of SiO_2 which has (001) cubic structure in this study. The honeycomb structures which can be seen in Figure 3.2 are developing roughness patterns. Since there are no removing honeycomb structures, this model is called a smooth pattern. Silicon molecules are represented in yellow color, and oxygen molecules are represented in red colors. The distance between silicon molecules in the y-direction is 5.063 Å, which equals 0.5063 nm.

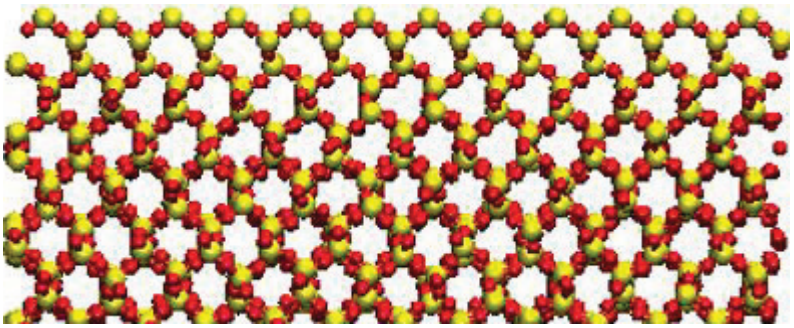

Figure 3.2. Honeycomb structres in smooth model

These nanopatterns are denoted as R_{xy} form. The reason is that removing honeycomb structures create roughness. In this form, x stands for the number of removed unit roughness element and y stands for the number of vertical silica layer which is subtracted. These patterns are shown in Figure 3.3. In addition, R00 is also called “Smooth Pattern”. Because nothing is removed in R00.

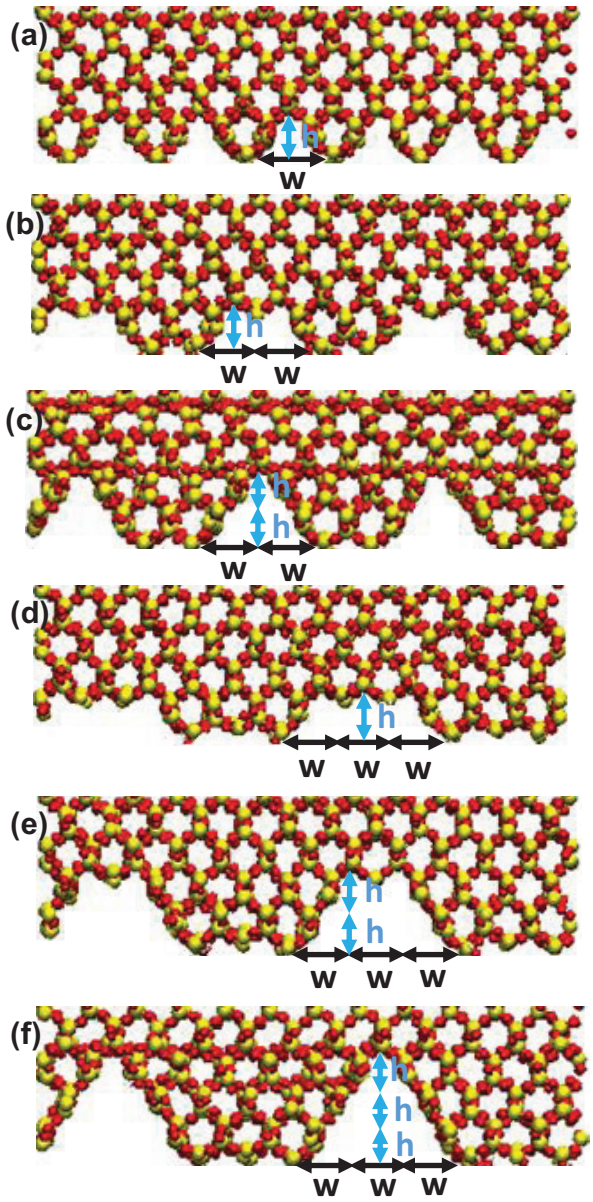

Figure 3.3. Notation of the surface models (a)R11, (b)R21, (c)R22, (d)R31, (e)R32, (f)R33

3.4. Ensembles

Ensembles of particles are one of the musts in molecular dynamics simulations to obtain feasible and efficient simulations. Besides bond length and bond angle of molecules, there are some needed macroscopic parameters and thermodynamic parameters in molecular dynamics simulation. These thermodynamic parameters are

temperature, pressure, volume, and energy. To define these parameters, ensembles must be used.

Common ensembles that are used in molecular dynamics simulations are NVE, NVT, NPT, and NPH. Each capital letter represents the constant component. These components; number of substances (N), volume (V), energy (E), pressure (P), temperature (T), and enthalpy (H). NVE is one of the statistical ensembles. The number of particles, volume, and energy are constant in NVE ensembles. If the number of particles, volume, and temperature of the system are kept constant, they are called NVT ensembles. Furthermore, if the number of particles, pressure, and temperature are kept constant, NPT is deployed. To keep the temperature constant in NVT and NPT, thermostats are used. In the literature, different types of thermostats are used such as the Nose-Hoover thermostat, Berendsen thermostat, and Anderson thermostat. Lastly, if the number of particles, total pressure, and total enthalpy of the system kept constant, the NPH ensemble is applied to the system.

3.5. Time Integration Algorithm in Molecular Dynamics

In MD simulation, the motion of the atoms with respect to time must be predicted. To do that, the initial position of atoms and interaction between atoms are considered. Commonly used algorithms for time integration in MD simulations are Euler[90], Verlet[91], Velocity Verlet[91], Leapfrog[92], and Beeman's[93] algorithm.

To derive all these algorithms, the derivative of the Taylor's expansion series is used. The first thing is to derive Taylor's expansion of position function with t+Δt. t is representing the time and Δt is representing the time step and shown in equation 3.8. After the position function is found, the first derivative of it with respect to time gives the velocity function and is shown in equation 3.9. Then, the first derivative of the velocity function with respect to time gives the acceleration function and is shown in equation 3.10.

$$r(t+\Delta t) = r(t) + v(t)\Delta t + \frac{1}{2}a(t)\Delta t^2 + \cdots \tag{3.8}$$

$$v(t+\Delta t) = v(t) + a(t)\Delta t + \frac{1}{2}b(t)\Delta t^2 + \cdots \tag{3.9}$$

$$a(t+\Delta t) = a(t) + b(t)\Delta t + \frac{1}{2}c(t)\Delta t^2 + \cdots \quad (3.10)$$

Time integration algorithms used in MD simulations are generally obtained by using equation 3.8, 3.9, and 3.10.

3.6. Simulation Details

In this thesis, silica, or called silicon dioxide (SiO_2) is used as solid walls. As shown in Figure 3.4, there are two parallel silica walls and there are liquid water molecules between silica walls. Total dimensions are 2.45, 6, and 14.2 nm in x, y, and z-direction. The simulation domain is containing 17520 atoms. The atomic weights of the silicon (Si), oxygen (O), and hydrogen (H) are 28.086, 15.9994, and 1.007970, respectively. Silica is modelled as (0, 0, 1) crystal plane cubic structure.

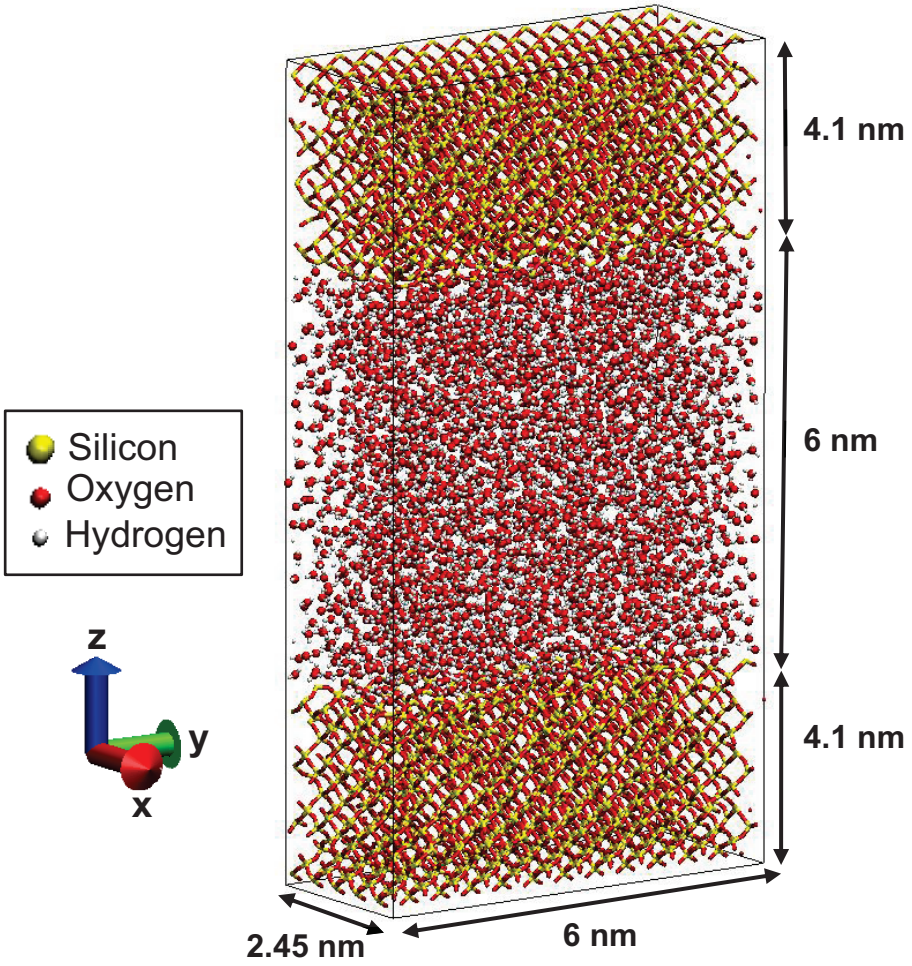

Figure 3.4. Nanopatterned surface model with dimensions in x-y-z direction

Water molecules are placed between silica molecules in the model. In order to create water molecules in the model, SPC/E water was used due to its low computational cost. Then, the SHAKE algorithm was applied to the water molecules. SHAKE algorithm was used to fix the bond length and bond angle in the model. The fixed bond length and bond angle parameters are 0.1 nm and 109.47 °. In short-range interactions between hydrogen and oxygen atom in water, van der Waals potential was used. However, in longe range interactions, Coulombic forces were used. As mentioned before, Coulobmic forces are computed by using Lennard-Jones potential. Van der Walls and Coulombic potentials in water molecules are set as 1 nm cut off distance and PPPM (Particle Particle Particle Mesh) was used as a solver to compute Coulomb potential. Similar atoms like H-H and O-O was calculated by combining Lennard Jones and Coulombic interactions which are equations 3.1 and 3.2. These parameters are obtained using the SPC/E model of water. However, the interaction parameters between silica and water at the molecular level must be computed. The interaction parameters between Si-Si are calculated by using Stillinger-Webber potential[94]. Also, the interaction parameters between O_S-O_W are calculated by using Density Functional Theory[94] (DFT). After these parameters were obtained, to calculate the interaction between Si-O, equation 3.3, and 3.4 were used. These equations are called as Lorentz-Berthelot mixing rule. Lorentz-Berhelot is simply taking the average of each interaction parameters. However, Barisik and Beskok[53] stated that this method is not precise to obtain actual parameters. The reason for this is that the calculated parameters by Lorentz-Berhelot mixing rules are $\sigma_{Si\text{-}O}$=2.6305 Å, and $\varepsilon_{Si\text{-}O}$=0.1288 eV. However, these parameters do not create wetting behavior. To solve this problem, 12.5% of the Lorentz-Berhelot mixing rule is applied. So, $\varepsilon_{Si\text{-}O}$=0.01511 eV parameter is used. Lastly, silica molecules are modelled by using Tersoff potential[95].

In this thesis, the calculations were applied for two different wetting conditions. We called that one is ε=1.0 which is the high wetting condition and the other one is ε=0.1 which is the low wetting condition. The interaction strength between O-O and Si-O was divided by 10 in ε=0.1 condition. The high wetting condition is denoted as ε=1.0, and the low wetting condition is denoted as ε=0.1. The molecular interaction parameters of ε=1.0 and ε=0.1 conditions are shown in Table 3.1 and Table 3.2, respectively.

Table 3.1. Molecular interaction parameters for high wetting condition, ε=1.0

Molecule Pair	σ (Å)	ε (eV)	q (e)
O-O	3.166	0.006739	-0.8476
H-H	0	0	0.4238
Si-O	2.633	0.01511	0

Table 3.2. Molecular interaction parameters for low wetting condition, ε=0.1

Molecule Pair	σ (Å)	ε (eV)	q (e)
O-O	3.166	0.0006739	-0.8476
H-H	0	0	0.4238
Si-O	2.633	0.001511	0

After the first model was developed, six more different model were designed. We had 7 different nanopatterned surface models in total. These models are shown in Figure 3.5.

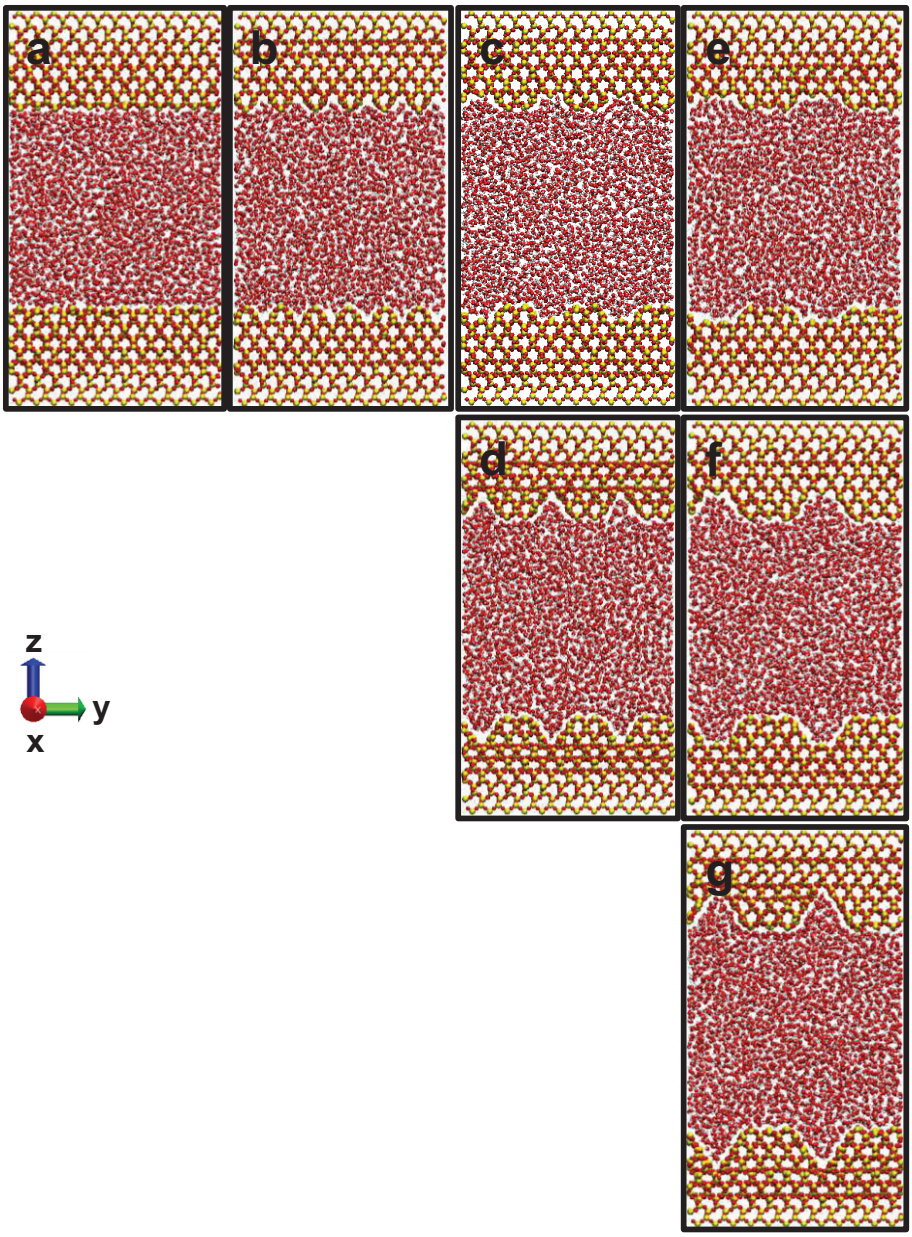

Figure 3.5. 7 nanopatterned surface models (a)R00-Smooth, (b)R11, (c)R21, (d)R22, (e)R31, (f)R32, (g)R33

These models were called R00, R11, R21, R22, R31, R32, and R33. Notations of these models have been explained in the previous section.

After these 7 nanopatterned surface models were created, the characterization of the simulation domain was started in MD. LAMMPS[96] (Large-scale Atomic/Molecular Massively Parallel Simulator) was used to characterize the model. LAMMPS is distributed as an open-source script. The size of the box which covered every atom in the model is specified. Also, information about atoms such as type, masses, number, locations, bond lengths, bond angles was written in the LAMMPS script. Then, boundary conditions and molecular interactions of atoms were added in the script. In the script, the

z-direction is divided by 300 slabs. Each slab has 0.0474 nm in the z-direction. Also, the y-direction is divided by 12 slabs. Each slab has 0.5 nm in the y-direction.

After the determination of all these parameters, ensembles were applied to the 7 nanopatterned surface models. Firstly, the Maxwell-Boltzman velocity distribution was applied to the model. Then, the Nose-Hoover thermostat was applied separately to the first three slabs and the last three slabs in z-direction to keep the wall temperature constant. After that, NVT ensemble was applied to obtain a thermodynamically equilibrium system at 323 K. When the system became to the equilibrium state, NVT was applied for the cold and hot layer at 283 K and 363 K, respectively. Then, NVE was applied to all systems except these cold and hot layers, and the thermostat region to obtain heat transfer between 283 K and 363 K in the system. As mentioned before, the Verlet time integration algorithm was used to apply these simulation parameters. The reason for this, Verlet time algorithm is simple, efficient, and stable. Also, it has a low CPU requirement. The time step which is used in Verlet algorithm was 0.001 ps. Note that, these ensembles are applied to the system by using the LAMMPS script. The basic schematic of the simulation domain is shown in Figure 3.6.

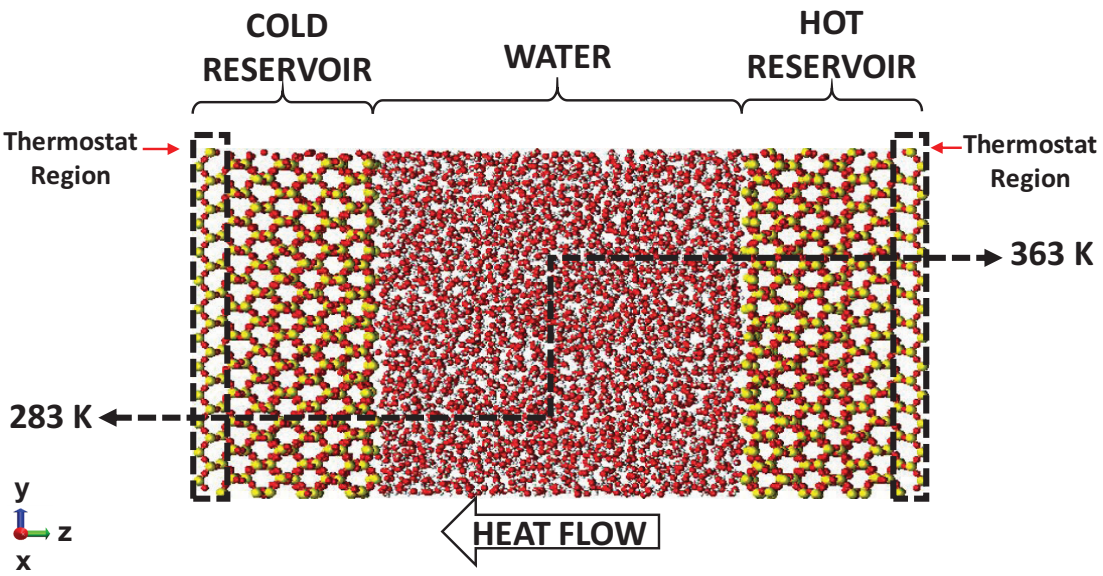

Figure 3.6. Basic schematic of the two-dimensional simulation domain.

Figure 3.6 is showing the schematic of the simulation domain of the R00 model as an example. However, all these simulation parameters were also applied to the other six models.

CHAPTER 4

RESULTS AND DISCUSSION

The starting point of the results of the thesis is the density distribution of water molecules and Si atoms. LAMMPS script gives the results as Ncount which is the number of atoms and density/number of atoms in a specific location for hydrogen, oxygen, and silicon. The density profiles were obtained in a thermodynamical equilibrium state at 323 K. After the calculations, density profiles of 7 nanopatterned surfaces and silicon are obtained for two different conditions; ε=1.0, and ε=0.1. Density profiles of R00, R11, R21, R22, R31, R32, R33, and silicon are represented in Figure 4.1 (a) for ε=1.0 condition, in Figure 4.1 (b) for ε=0.1 condition. There are two main purposes for obtaining density profiles. The first one is the comparison of simulation density data and theoretical density values. The other one is the observation of the behavior of water and silicon density for 7 different surface models for two conditions. Theoretical density values of water and silicon are 1.006 g/cm^3 and 2.36 g/cm^3. According to simulation results, the average density of water and silicon was observed as 1.03 g/cm^3 and 2.35 g/cm^3, respectively. It means that simulation results were matched with theoretical values. Also, the behavior of density profiles for different models was observed. As shown in Figure 3.2, these 7 nanostructures have different surface patterns. Normally water molecules are placed between 4 and 10 nm in the R00 model. Since R33 has the biggest cavity volume, water molecules are started from 3.345 nm. It means that the solid-liquid interface is placed in that location. Since R00 has no cavity volume, the solid-liquid interface is located at 4 nm. These 7 nanopatterned silica structures have a solid-liquid interface with different locations. In other words, the starting and ending locations of the hot and cold reservoir are different in these 7 models. In addition, the density profile of water and silicon is not much changing between ε=1.0 and ε=0.1 conditions, according to Figure 4.1 (a) and 4.1 (b). Also, the water density peaks at the cold reservoir are higher than the hot reservoir for two different conditions.

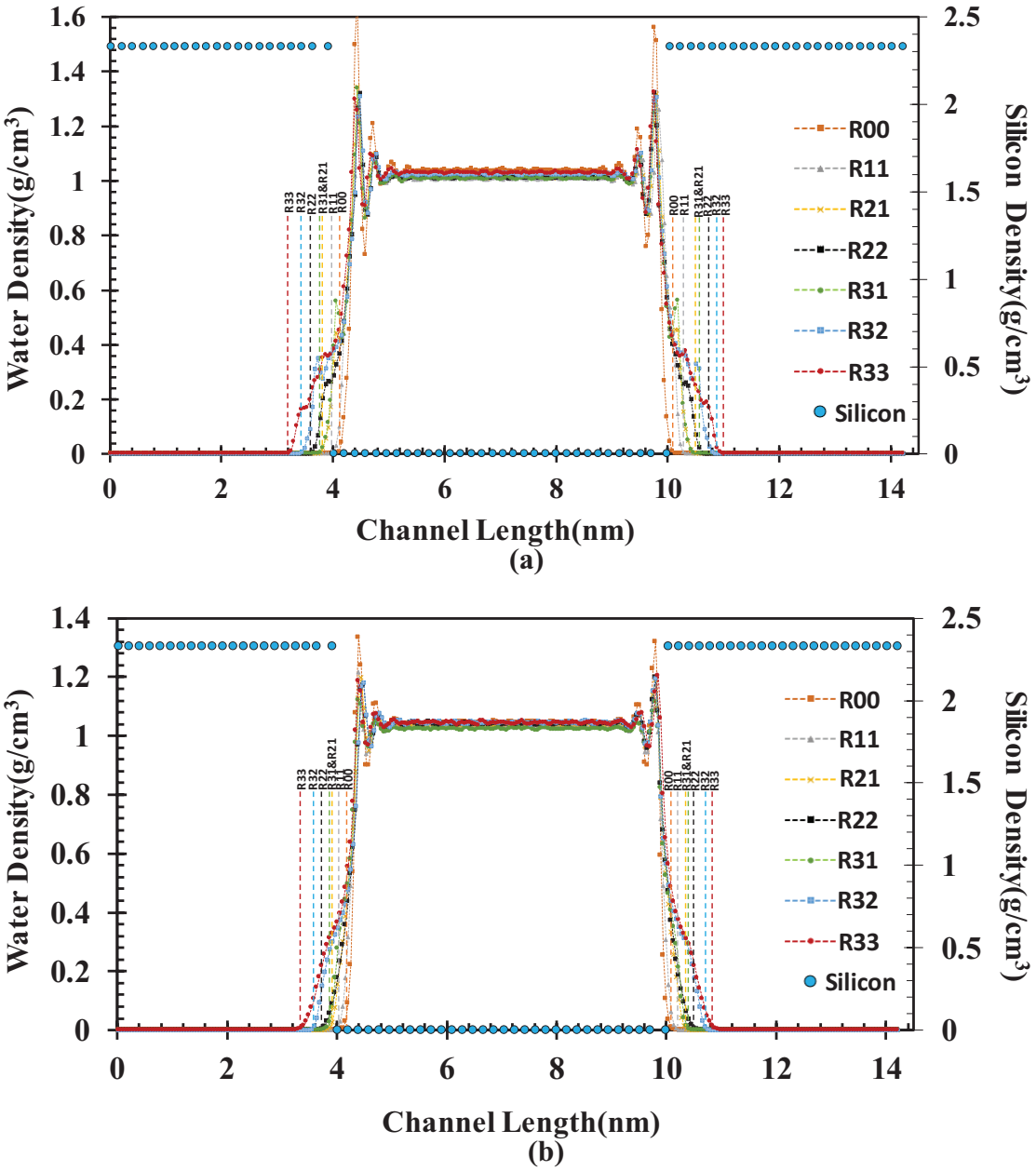

Figure 4.1. Density profiles of all models for (a) ε=1.0 condition, and (b) ε=0.1 condition.

After one-dimensional density profiles of water molecules and silicon were obtained in the z-direction, two-dimensional (y-z) density distribution of the seven nanopatterned surface models have been created. Figure 4.3 shows the two-dimensional density distribution of all models within the range of 0 and 4.8 gr/cm^3. After one-dimensional density profiles and two-dimensional density distribution of seven models were obtained, the two-dimensional temperature distribution of seven models has been created to investigate heat transfer more clearly within the range of 283 and 363 K and shown in Figure 4.4. According to color saturation, the temperature of the cold reservoir

is within the range of 283 and 288 K, the temperature of the water is within the range of 304 and 336 K, and the temperature of the hot reservoir is within the range of 358 and 363 K. Also, different colors are obsorved at the interface of the models. It means that there are temperature jumps at the solid-liquid interface in the cold and hot reservoir.

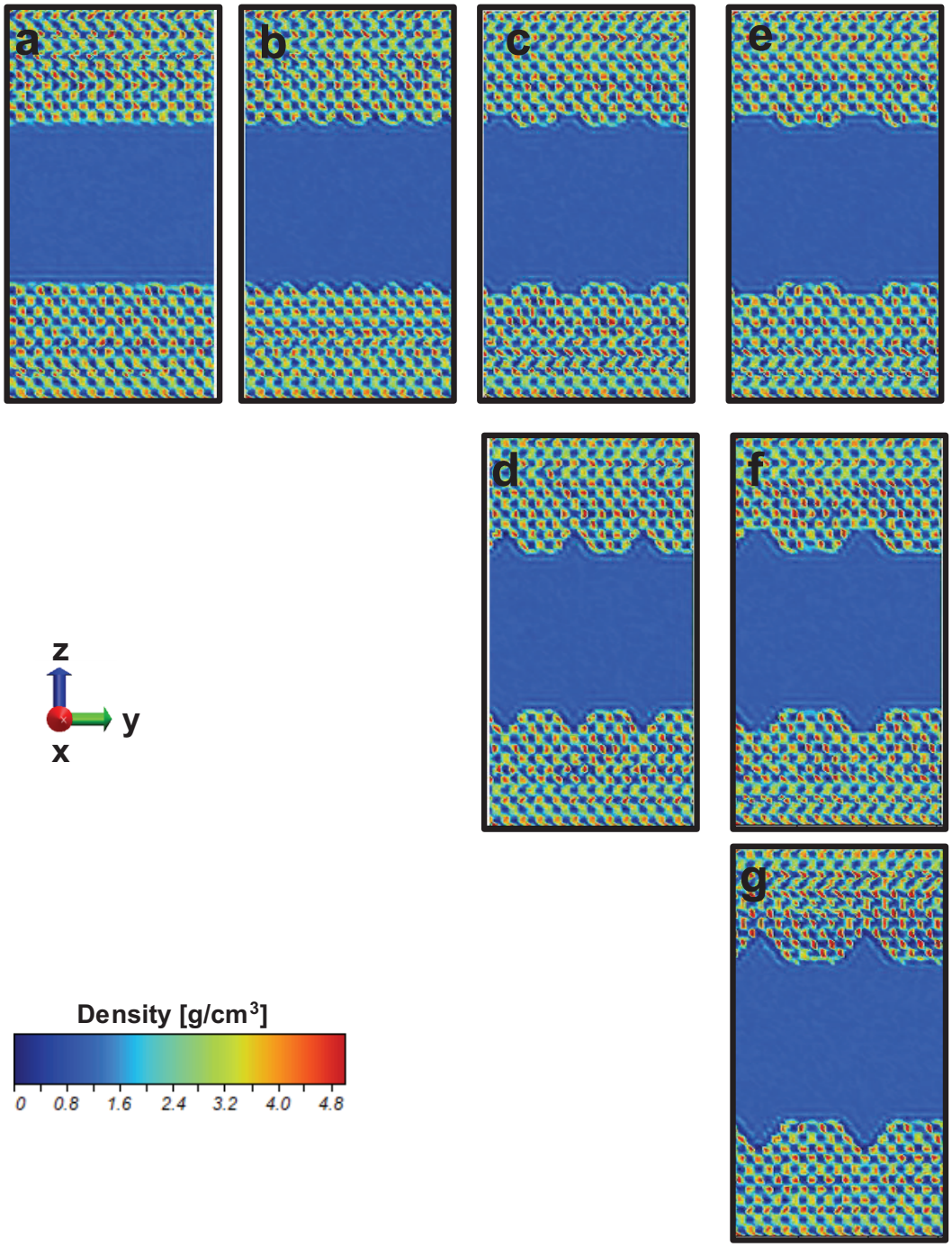

Figure 4.2. 2D Density Distribution of 7 nanopatterned surface models (a)R00-Smooth, (b)R11, (c)R21, (d)R22, (e)R31, (f)R32, (g)R33

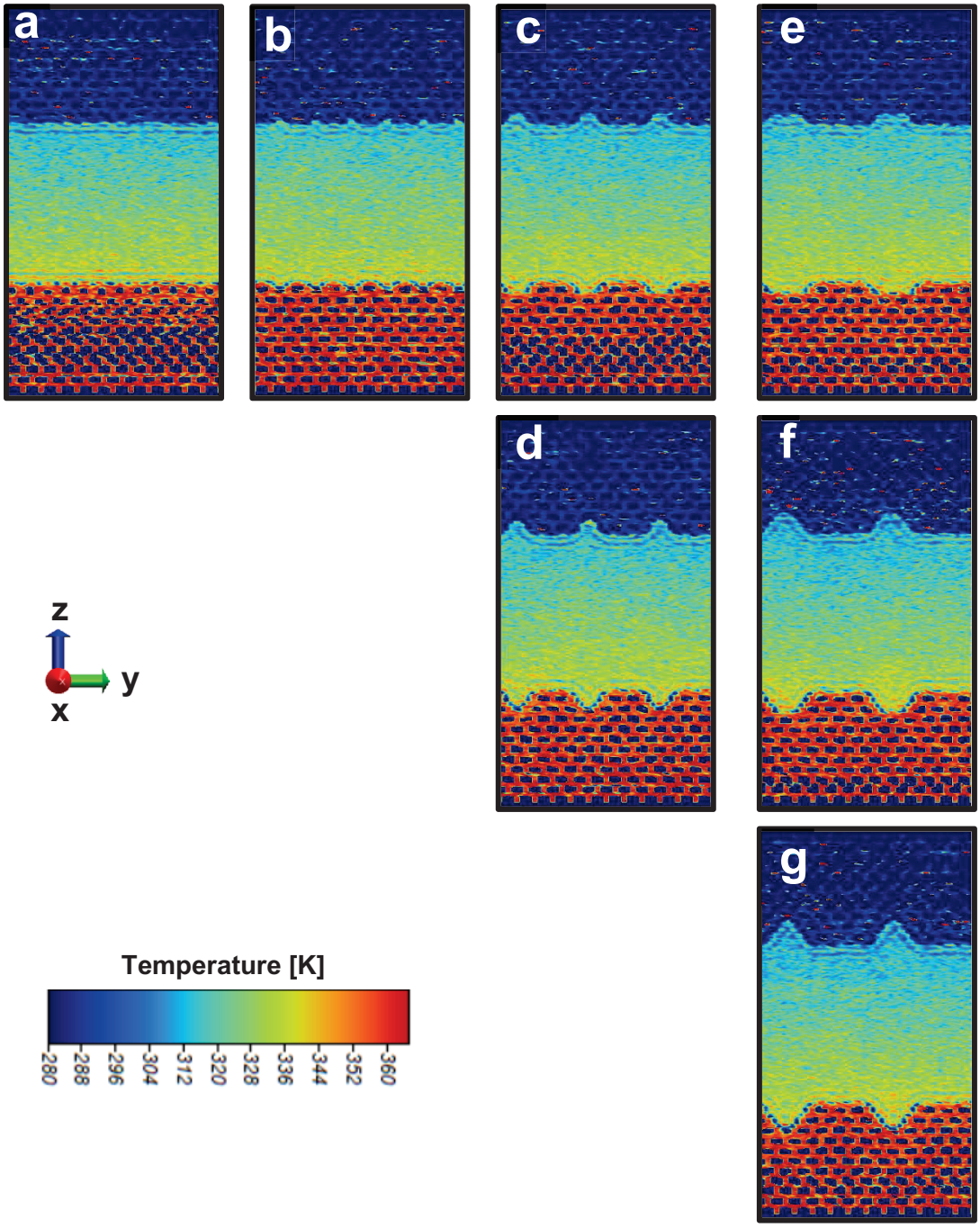

Figure 4.3. 2D Temperature Distribution of 7 nanopatterned surface models (a)R00-Smooth, (b)R11, (c)R21, (d)R22, (e)R31, (f)R32, (g)R33

Temperature distributions were obtained in silica-water-silica model within temperature difference 283 K and 363 K for ε=1.0 and ε=0.1 conditions and illustrated in Figure 4.4. The temperature profiles vary with the surface structure of the models for ε=1.0 condition and ε=0.1 condition. Nose-Hoover thermostat applied to first three slabs

and last three slabs of the model. Note that, z-direction was divided by 300 pieces and these pieces are called slabs. In other words, between 0 and 0.12 nm and between 14.08 and 14.2 nm there are thermostats applied. Silica temperatures vary linearly except near the interface at the cold and hot reservoir for all models. Also, silica and water molecules interacted early in the R33 model due to cavity volume. Temperature jumps were observed at the interface due to thermal velocity difference. These temperature jumps are represented as Kapitza length or interfacial thermal resistance. Kapitza length is caused by a mismatch in the phonon spectrum. It is a function of the temperature gradient of the liquid and the temperature jump at the interface. The formulation of Kapitza length is given in equation 2.1. The temperature gradient of the liquid in the ε=1.0 condition is higher than the ε=0.1 condition. The average water temperature gradients of seven nanopatterned surface structures for ε=1.0 condition is 3.61, 3.63, 3.45, 3.6, 3.56, 3.58, and 3.74 for R00, R11, R21, R22, R31, R32, and R33, respectively. In ε=0.1 condition, the average water temperature gradient of seven nanopatterned surface structures are 1.1, 0.9, 1.03, 1.11, 0.97, 1.53, and 1.3, respectively. The difference between the water temperature gradient can be seen clearly in Figure 4.4 (a) and 4.4 (b) for different conditions. Also, the temperature jumps for the ε=1.0 condition are lower than the ε=0.1 condition. These results prove that Kapitza length values of ε=1.0 condition are lower than ε=0.1 condition.

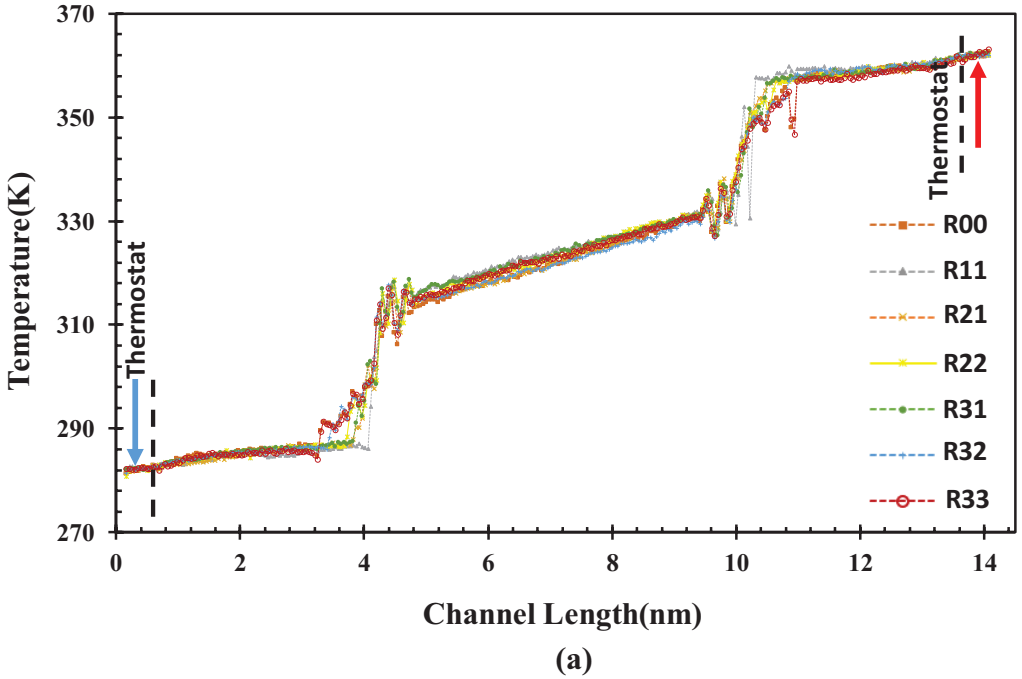

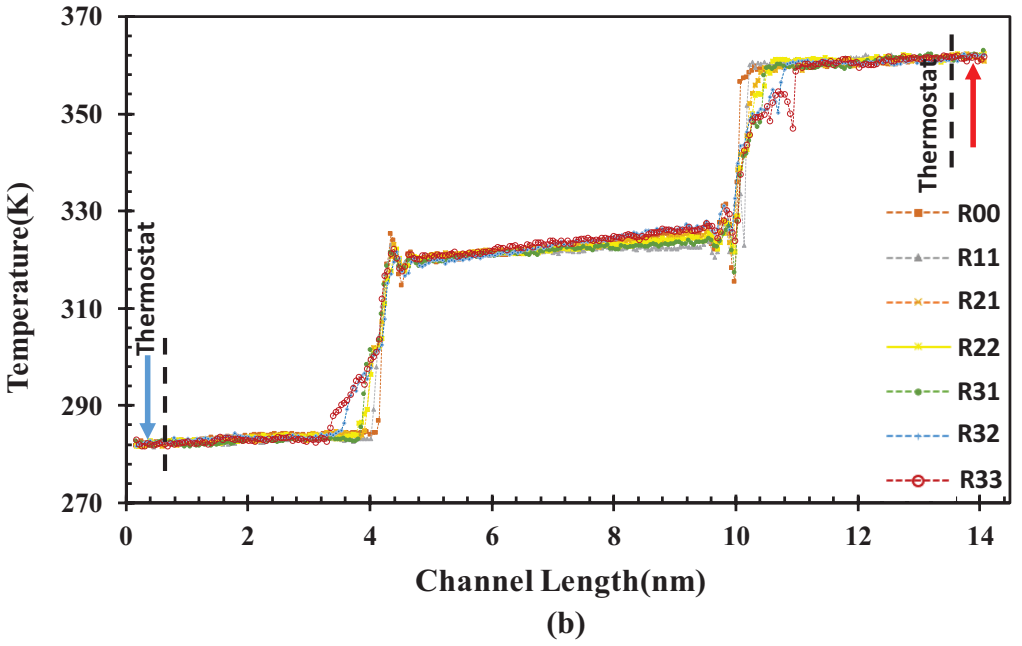

Figure 4.4. Temperature profiles of all models for (a) ε=1.0 condition, and (b) ε=0.1 condition.

One-dimensional temperature profiles for ε=1.0 and ε=0.1 conditions are illustrated in Figure 4.4 in general. However, to investigate the temperature profiles detailly, R11, and R33 nanopatterned surface structures are used. The one-dimensional temperature profiles of R11 and R33 for ε=1.0 condition is illustrated in Figure 4.5. As

mentioned before, the y-direction is divided into 12 layers. In the R11 model, these 12 layers are represented as T1, B1, T2, B2, T3, B3, T4, B4, T5, B5, T6, and B6. The capital letter “T” is denoted as the top section of the wall. The capital letter “B” is denoted as the bottom section or cavity section of the wall. The temperature profile and representation of the layers are shown in Figure 4.5 (a) for the R11 model. The measured average temperature gradient of the water in the top section is 3.6407. The temperature jumps at the silica-water interface in the cold and hot reservoirs at the top section are 24.23 K and 21.29 K, respectively. In the bottom section, the average temperature gradient is measured as 3.6049. The temperature jumps at the silica-water interface in the cold and hot reservoirs at the bottom section are 25.05 K and 22.09 K, respectively. The water temperature in the top section started at 312.45 K and ended at 335.94 K. In the bottom section, it started at 313.22 K and ended at 335.12 K. These results showed that the temperature jump at the cold reservoir is higher than the hot reservoir. However, the temperature jumps are higher in the bottom section. The temperature gradient of the bottom section is a bit lower than the top section. In the R33 model, 12 layers are represented as B1, B2, B3, T1, T2, T3, B4, B5, B6, T4, T5, and T6. B1, B3, B4, and B6 are the higher locations of the cavity. However, B2 and B5 are the deepest locations of the cavity. T1, T2, T3, T4, T5, and T6 are the top section of the R33 model. The temperature profile and representation of the layers are shown in Figure 4.5 (b) for the R33 model. The average water temperature gradient of the higher locations of the cavity which are B1, B3, B4, and B6 layers is 3.7084. The average temperature jumps of cold and hot reservoirs at these layers are 19.89 K and 21.24 K, respectively. In the deepest locations of the cavity which are B2 and B5 layers, the average temperature gradient is 3.7767. The temperature jumps of these deepest locations of the cavity of cold and hot reservoirs are 21.74 K and 22.46 K, respectively. In the top section which are T1, T2, T3, T4, T5, and T6 layers, the average temperature gradient is calculated as 3.7507. The temperature jumps of cold and hot reservoirs in these layers are 18.99 K and 20.39 K, respectively. These results showed that the deepest point of the cavity has the highest water temperature gradient. Also, the temperature jump of hot reservoirs is higher than cold reservoirs in the R33 model. The deepest locations of the cavity have the highest temperature jump values. If R11 and R33 are compared to each other, the temperature jumps of the cold and hot reservoirs decreased in R33.

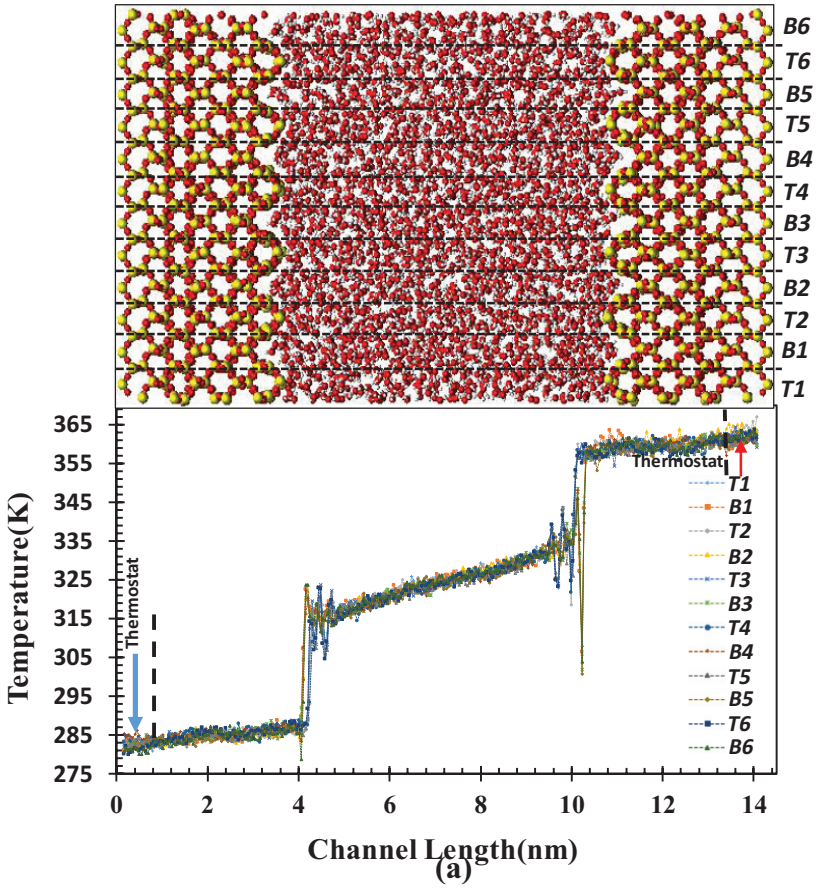

Figure 4.5. 1D Temperature profiles of R11 and R33 for ε=1.0 conditions are (a), (b), respectively.

In ε=0.1 condition, similar layer representation for R11 and R33 in ε=1.0 condition is used. Figure 4.6 (a) shows the temperature profile of the R11 model for the ε=0.1 condition. In the R11 model, the average water temperature gradient of the top and bottom layers are calculated as 0.905, 0.9018, respectively. It showed that the average water temperature gradient is not much changing between the top and bottom layers. But these values are almost one-fourth of the water temperature gradient of the R11 model in ε=1.0 condition. The temperature jumps of cold and hot reservoirs at top sections are 35.16 K and 34.99 K, respectively. In the bottom sections, the temperature jumps of cold and hot reservoirs at the top sections are 35.28 K and 34.93 K, respectively. Again, it showed that the temperature jumps of the cold reservoir are higher than the hot reservoir in the R11 model. Also, the temperature jumps are much higher compared to the ε=1.0 condition. The water temperature in the top section started at 318.84 K and ended at 324.85 K. In the bottom section, it started at 318.99 K and ended at 324.68 K. Figure 4.6 (b) shows the temperature profile of the R33 model for ε=0.1 condition. In the R33 model, the average water temperature gradient of the higher locations of the cavity is 1.3609. The temperature jumps of cold and hot reservoirs at these locations are 33.21 K and 31.95 K, respectively. In the deepest locations of the cavity, the water temperature gradient is calculated as 1.2417 and temperature jumps of the cold and hot reservoir at these locations are 33.91 K and 32.86 K, respectively. In top layers, the average water temperature gradient is 1.2783, and temperature jumps of the cold and hot reservoir at these locations are 32.89 K and 31.68 K, respectively. Temperature jumps decreased in the R33 model. However, they are much higher than the R33 model for the ε=1.0 condition. In addition, the average water temperature gradient of the R33 model is greater than the R11 model for ε=0.1 condition.

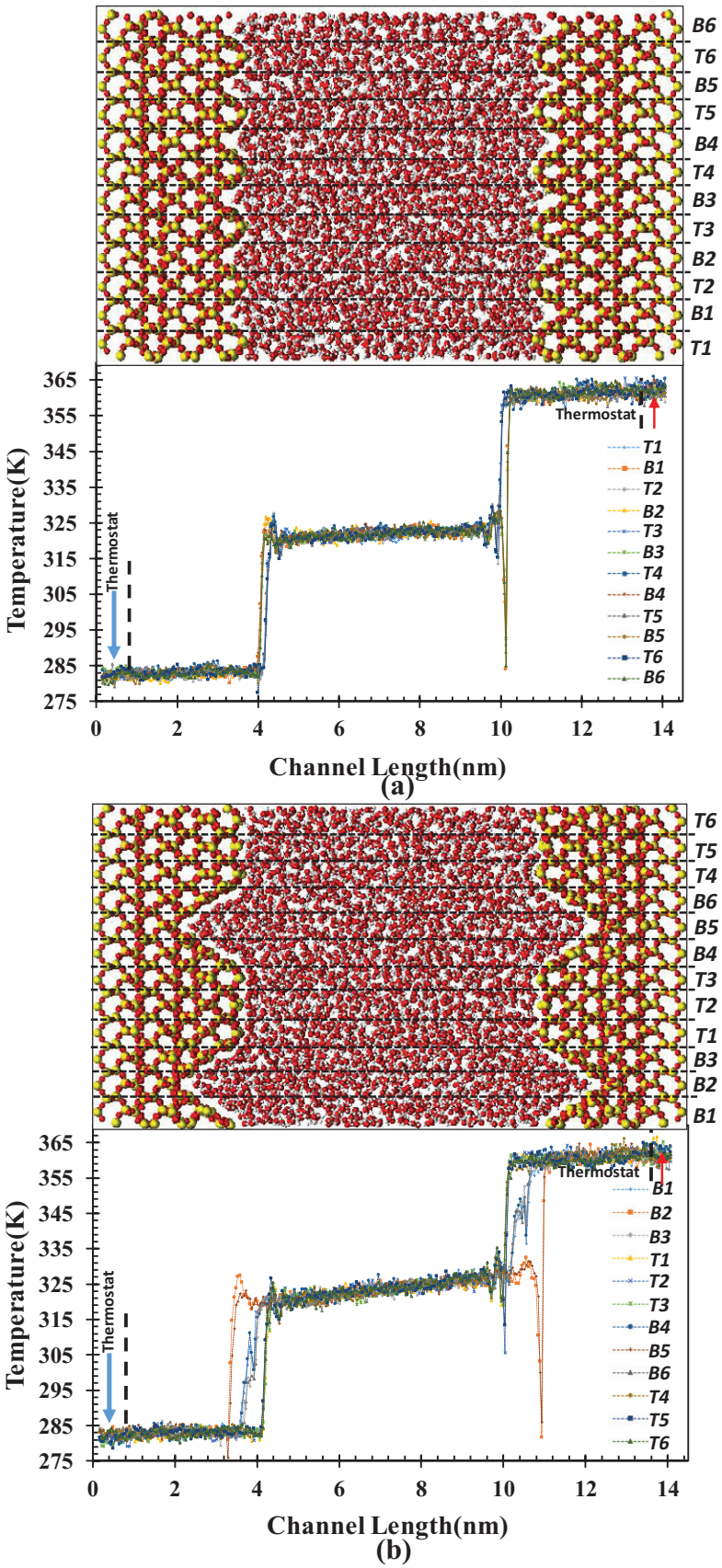

Figure 4.6. 1D Temperature profiles of R11 and R33 for ε=0.1 condition is (a), (b), respectively.

Figure 4.5 and 4.6 shows the temperature profiles of R11 and R33 for ε=1.0 condition and ε=0.1 condition. However, the same calculations are done to other models for two different conditions. After the average temperature gradient of water and the temperature jumps of the cold and hot reservoir of all models for two conditions, Kapitza length can be calculated. In this thesis, two different Kapitza length values are calculated for the silica-water interface of the cold reservoir and hot reservoir. Kapitza length of the cold reservoir is denoted as $L_{K\text{-}COLD}$, and the hot reservoir is denoted as $L_{K\text{-}HOT}$. The needed parameters for calculating Kapitza length are given in equation 2.1. 12 Kapitza length values for 12 layers are calculated for ε=1.0 condition and ε=0.1 condition. The calculated Kapitza length values for the ε=1.0 condition are shown in Figure 4.7 and the ε=0.1 condition is shown in Figure 4.8. Both values in Figures 4.7 and 4.8 are the average values of repetitive layers. As an example, in the R11 model, bottom layers which are B1, B2, B3, B4, B5, and B6, and top layers which are T1, T2, T3, T4, T5, and T6 are repeated layers. However, in the R33 model, all the top layers are repetitive. Also, both B2 and B5 are the deepest point of the cavity. So, these are also repetitive. The remaining layers such as B1, B3, B4, and B6 are higher locations of the cavity. So, these are also repetitive layers. Average Kapitza length values of the repetitive layers with respect to channel width are represented in these figures.

In the ε=1.0 condition, Kapitza length values are calculated for R00, R11, R21, R22, R31, R32, and R33. In the R00 pattern, also called a smooth pattern, there are no cavities. The calculated Kapitza length values at the silica-water interface for cold and hot reservoirs are 6.72 nm and 6.36 nm, respectively. In the R11 pattern, some of the layers are repetitive as mentioned before. In the cavity section, Kapitza lengths at the silica-water interface for cold and hot reservoirs are calculated as 6.65 nm and 5.84 nm, respectively. In top layers, it is measured as 6.95 nm for the cold reservoir, and 6.12 nm for the hot reservoir. In the R21 pattern, $L_{K\text{-}COLD}$, and $L_{K\text{-}HOT}$ values of the cavity section are 6.86 nm and 6.30 nm, respectively. In top layers, calculated $L_{K\text{-}COLD}$, and $L_{K\text{-}HOT}$ values are 7.18 nm and 6.65 nm, respectively. In the R22 pattern, $L_{K\text{-}COLD}$, and $L_{K\text{-}HOT}$ values are calculated as 6.10 nm and 5.85 nm for the cavity section. In top layers, $L_{K\text{-}COLD}$, and $L_{K\text{-}HOT}$ values are calculated as 6.25 nm and 6.16 nm, respectively. In the R31 pattern, the first three layers are in the cavity section. The next three layers are the top layers. In cavity layers, calculated $L_{K\text{-}COLD}$, and $L_{K\text{-}HOT}$ values are 6.88 nm and 6.12 nm, respectively. In top layers, calculated $L_{K\text{-}COLD}$, and $L_{K\text{-}HOT}$ values are 7.66 nm and 6.85

nm, respectively. In the R32 pattern, a similar approach in the R33 pattern is used to calculate Kapitza length. $L_{K\text{-}COLD}$ and $L_{K\text{-}HOT}$ values for higher locations in the cavity are 6.13 nm and 6.22 nm, respectively. In the deepest location of the cavity, calculated $L_{K\text{-}COLD}$, and $L_{K\text{-}HOT}$ values are 5.74 nm and 5.89 nm, respectively. In top layers, $L_{K\text{-}COLD}$, and $L_{K\text{-}HOT}$ values are calculated as 6.55 nm and 6.64 nm, respectively. In the R33 pattern, calculated $L_{K\text{-}COLD}$, and $L_{K\text{-}HOT}$ values for higher locations in the cavity are 5.36 nm and 5.79 nm, respectively. In the deepest location of the cavity, $L_{K\text{-}COLD}$, and $L_{K\text{-}HOT}$ values are calculated as 5.06 nm and 5.43 nm, respectively. In top layers, calculated $L_{K\text{-}COLD}$, and $L_{K\text{-}HOT}$ values are 5.75 nm and 5.94 nm, respectively. These results showed that $L_{K\text{-}COLD}$ is greater than $L_{K\text{-}HOT}$ except for R32 and R33 patterns. Also, Kapitza length of the top layers is greater than Kapitza length of the cavity section. The deepest locations of the pattern have the lowest Kapitza length values.

In the ε=0.1 condition, Kapitza length values are also calculated for R00, R11, R21, R22, R31, R32, and R33. In the ε=0.1 condition, the molecular interaction strengths between O-O, H-H, and Si-O are ten times lower than the ε=1.0 condition. Because of lower interaction strengths, Kapitza lengths are expected much higher in the ε=0.1 condition. In the R00 pattern, $L_{K\text{-}COLD}$, and $L_{K\text{-}HOT}$ values are calculated as 30.96 nm and 30.71 nm, respectively. In the R11 pattern, Kapitza lengths of the cavity section for cold and hot reservoiors are 38.85 nm and 38.66 nm, respectively. In top layers, calculated $L_{K\text{-}COLD}$, and $L_{K\text{-}HOT}$ values are 39.12 nm and 38.74 nm, respectively. In the R21 pattern, Kapitza lengths of the cavity section for cold and hot reservoirs are 33.03 nm and 31.17 nm, respectively. In top layers, calculated $L_{K\text{-}COLD}$, and $L_{K\text{-}HOT}$ values are 35.33 nm and 33.58 nm, respectively. In the R22 pattern, $L_{K\text{-}COLD}$, and $L_{K\text{-}HOT}$ values are calculated as 30.96 nm and 29.95 nm for the cavity section. In top layers, $L_{K\text{-}COLD}$, and $L_{K\text{-}HOT}$ values are calculated as 31.50 nm and 30.34 nm, respectively. In the R31 pattern, similar cavity layers and top layers approach is used like in the R31 model in ε=1.0 condition. In cavity layers, calculated $L_{K\text{-}COLD}$, and $L_{K\text{-}HOT}$ values are 35.12 nm and 37.91 nm, respectively. In top layers, calculated $L_{K\text{-}COLD}$, and $L_{K\text{-}HOT}$ values are 34.3 nm and 37.26 nm, respectively. In the R32 pattern, $L_{K\text{-}COLD}$, and $L_{K\text{-}HOT}$ values for higher locations in the cavity are 22.49 nm and 20.16 nm, respectively. In the deepest location of the cavity, calculated $L_{K\text{-}COLD}$, and $L_{K\text{-}HOT}$ values are 22.54 nm and 20 nm, respectively. In top layers, $L_{K\text{-}COLD}$, and $L_{K\text{-}HOT}$ values are calculated as 21.42 nm and 19.36 nm, respectively. In the R33 pattern, calculated $L_{K\text{-}COLD}$, and $L_{K\text{-}HOT}$ values for higher locations in the cavity are

24.4 nm and 23.48 nm, respectively. In the deepest location of the cavity, $L_{K\text{-}COLD}$, and $L_{K\text{-}HOT}$ values are calculated as 25.73 nm and 24.78 nm, respectively. In top layers, calculated $L_{K\text{-}COLD}$, and $L_{K\text{-}HOT}$ values are 27.31 nm and 26.46 nm, respectively. These results showed that $L_{K\text{-}COLD}$ is greater than $L_{K\text{-}HOT}$ except for the R31 pattern. Also, Kapitza length values are much greater in the ε=0.1 condition compared to the ε=1.0 condition. The reason for this, weaker interactions create higher temperature jumps and lower water temperature gradients in the system. However, $L_{K\text{-}COLD}$ and $L_{K\text{-}HOT}$ values for the cavity section are greater than the top layers in R31 and R32 patterns. Also, the deepest points of the cavity have the highest $L_{K\text{-}COLD}$ values in the R32 pattern.

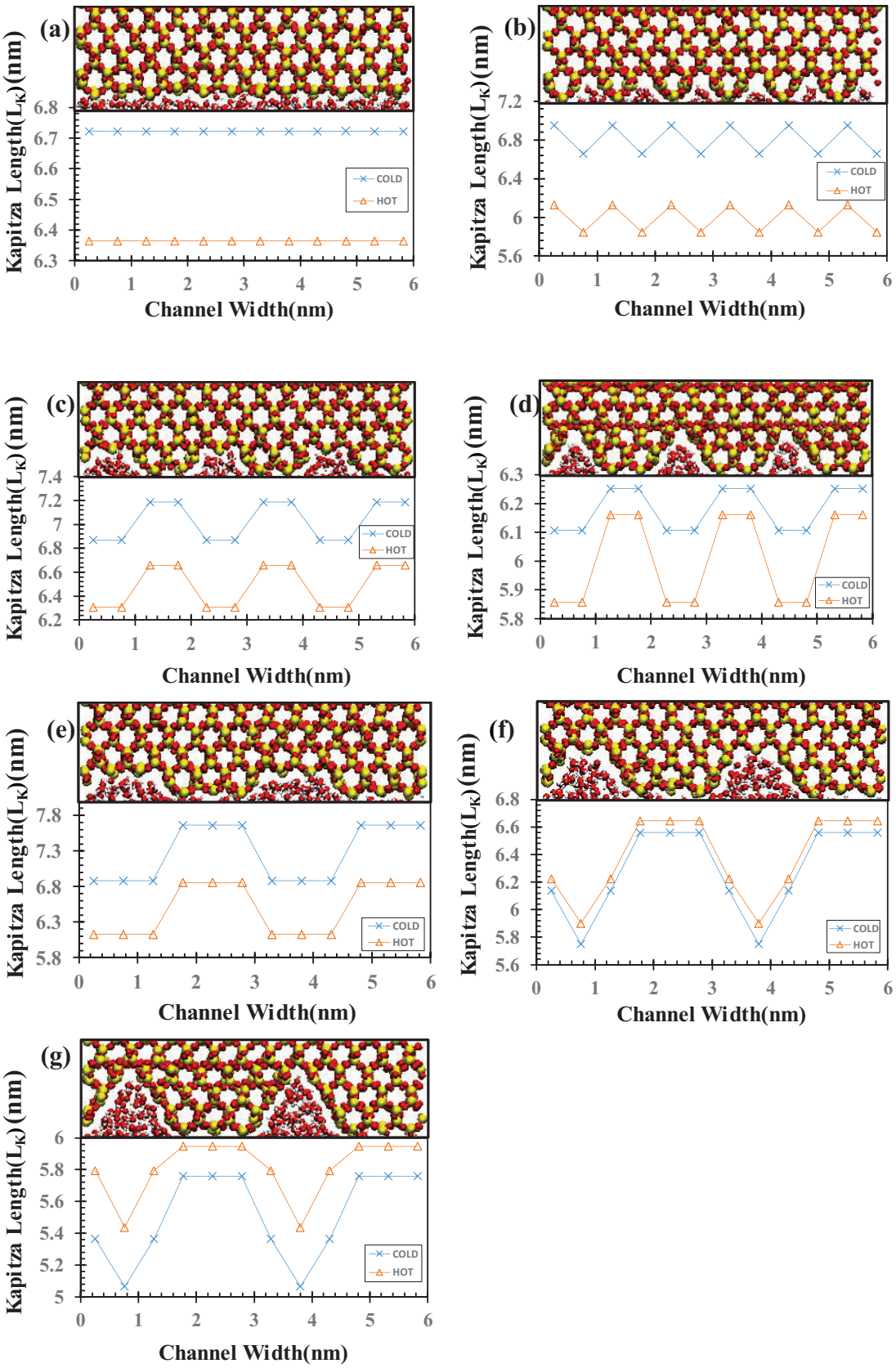

Figure 4.7. Kapitza Length values of 7 nanopatterned surface models for ε=1.0 condition. (a)R00-Smooth, (b)R11, (c)R21, (d)R22, (e)R31, (f)R32, (g)R33

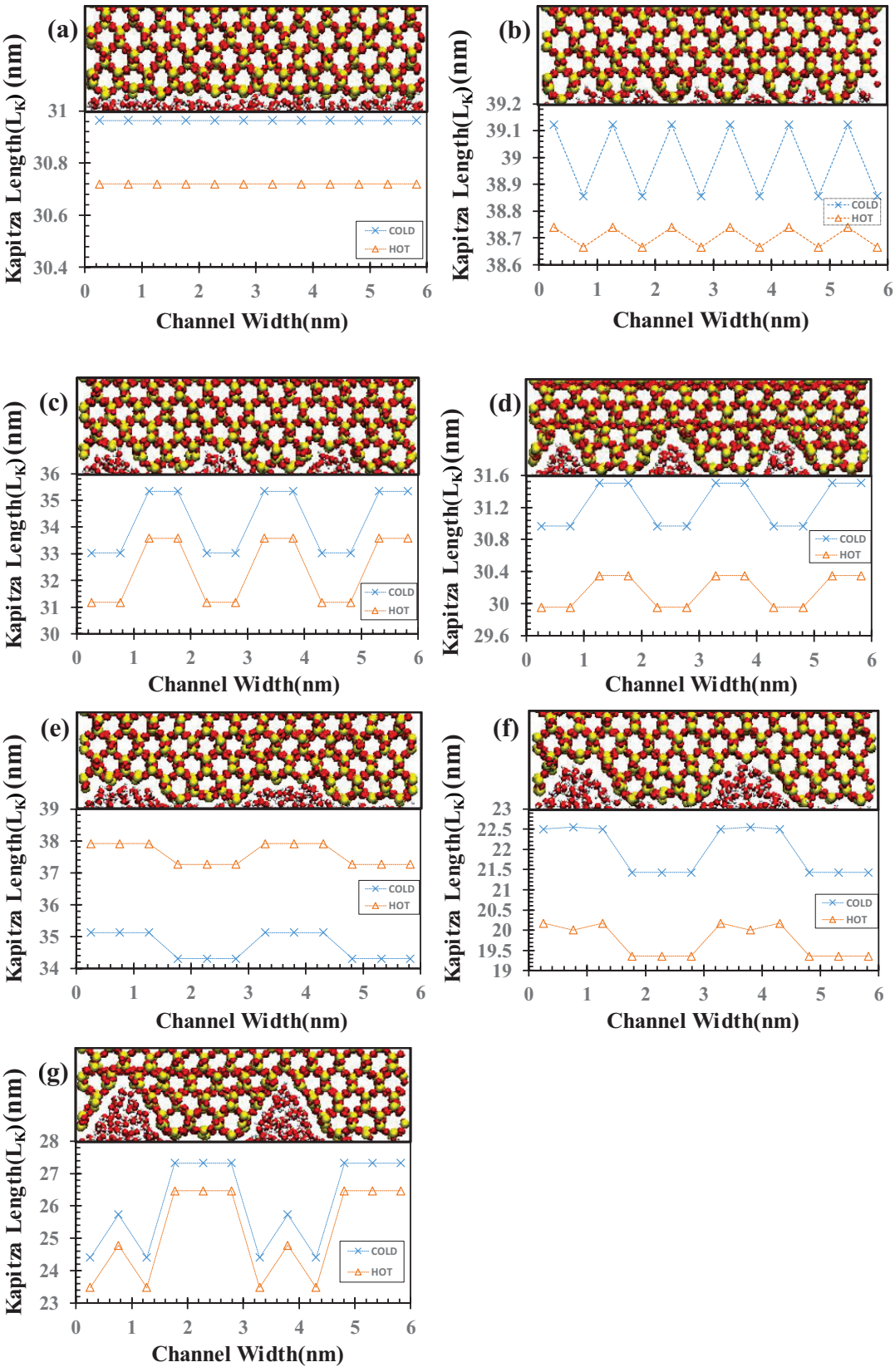

Figure 4.8. Kapitza Length values of 7 nanopatterned surface models for ε=0.1 condition. (a)R00-Smooth, (b)R11, (c)R21, (d)R22, (e)R31, (f)R32, (g)R33

Previous results showed the $L_{K\text{-}COLD}$ and $L_{K\text{-}HOT}$ values for 7 nanopatterned surface structures and two different molecular interaction strength parameters. To observe the effect of the volume of the cavity, the unit crystal cavity volume parameter is defined. This parameter is denoted as V_c and found by multiplication of cavity height, cavity width, and cavity length. Figure 4.9 shows the number of unit crystal cavity volume which is extracted from R11, R21, R22, R31, R32, and R33 patterns. The red-colored hexagons represented V_c. In R11, only one V_c is extracted from the pattern. In R21, there are two V_c that is removed from the pattern. In R22 and R31, there are three V_c that is removed from the pattern. Also, the number of removed V_c for R32 and R33 patterns are five and six, respectively. After the number of removed V_c for each model obtained, the effects of the removed V_c on Kapitza length are achieved. Figure 4.10 shows the changing of Kapitza length with respect to the number of V_c for ε=1.0 condition, and ε=0.1 condition. However, since R22 and R31 patterns have the same number of removed V_c, this makes Figure 4.10 complicated. For the ε=1.0 condition which is shown in Figure 4.10 (a), Kapitza length has a peek point at V_c equals 3. This peek point belongs to the R31 pattern. The lowest Kapitza length values are observed when V_c equals 6 which belongs R33 pattern. If Kapitza length values of the R22 condition are ignored, Kapitza length values are increasing until V_c equals 3. After this point, they are decreasing. For the ε=0.1 condition which is shown in Figure 4.10 (b), the highest Kapitza length values are observed at V_c equals 1. The lowest Kapitza length values are observed when V_c is 5. If Kapitza length values of R31 condition are ignored in ε=0.1 condition, Kapitza length values are decreasing until V_c equals 5, then increasing.

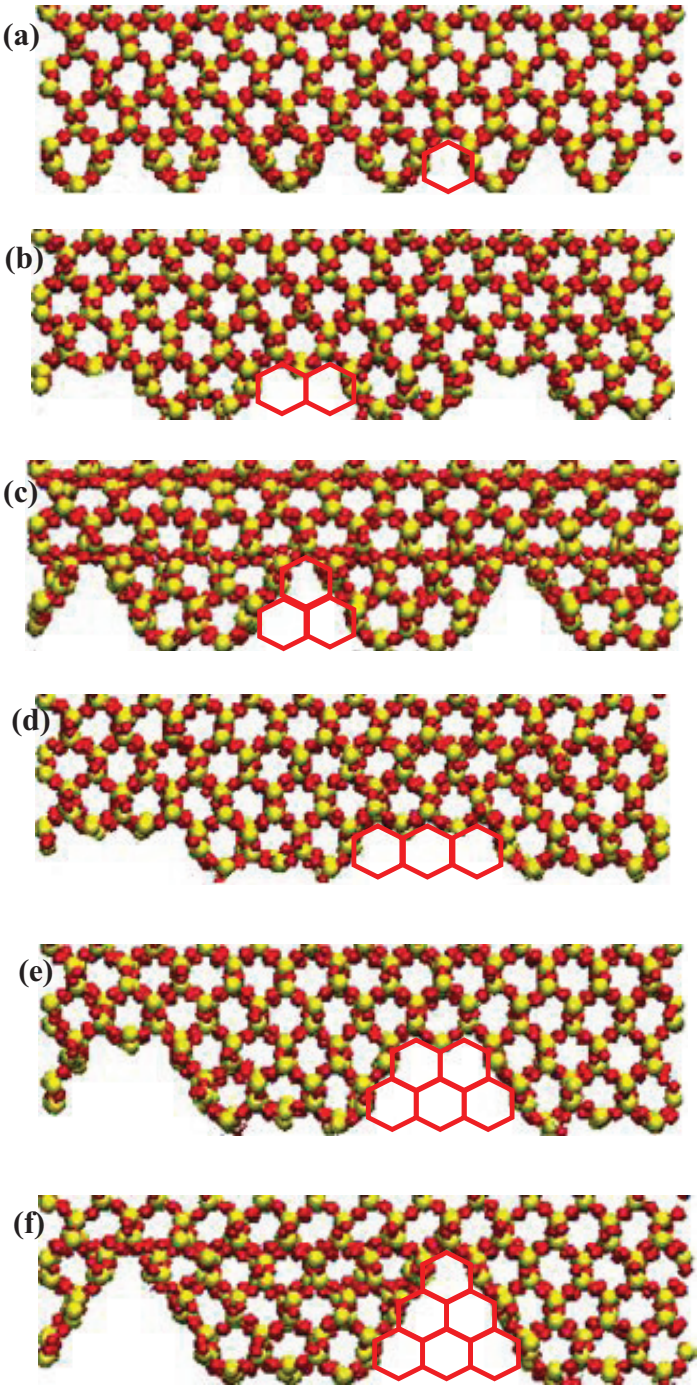

Figure 4.9. Unit crystal cavity volume extraction of 7 nanopatterned surfaces. (a)R11, (b)R21, (c)R22, (d)R31, (e)R32, (f)R33

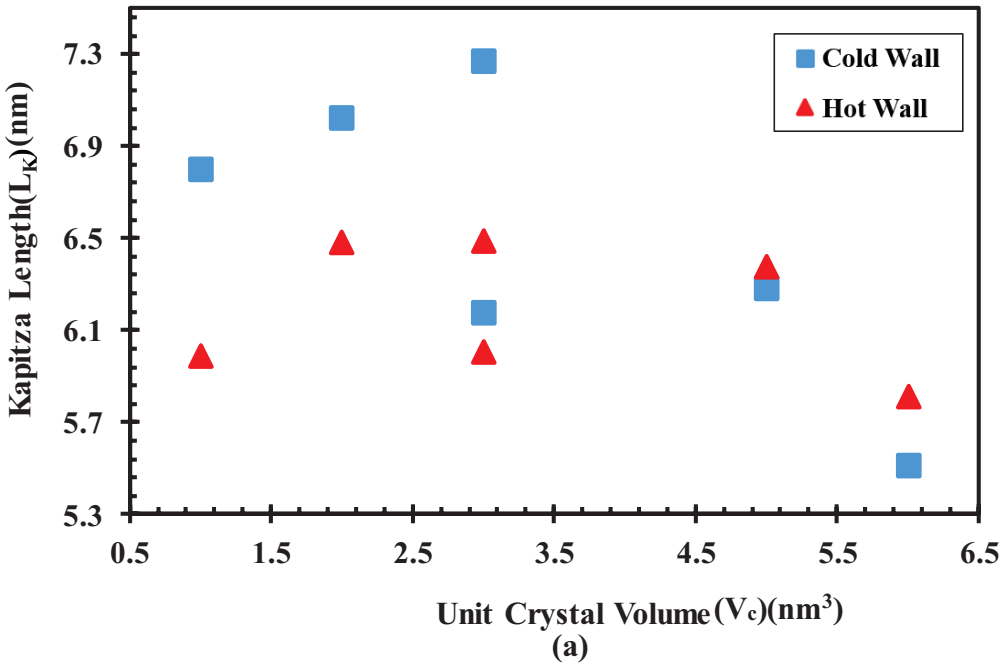

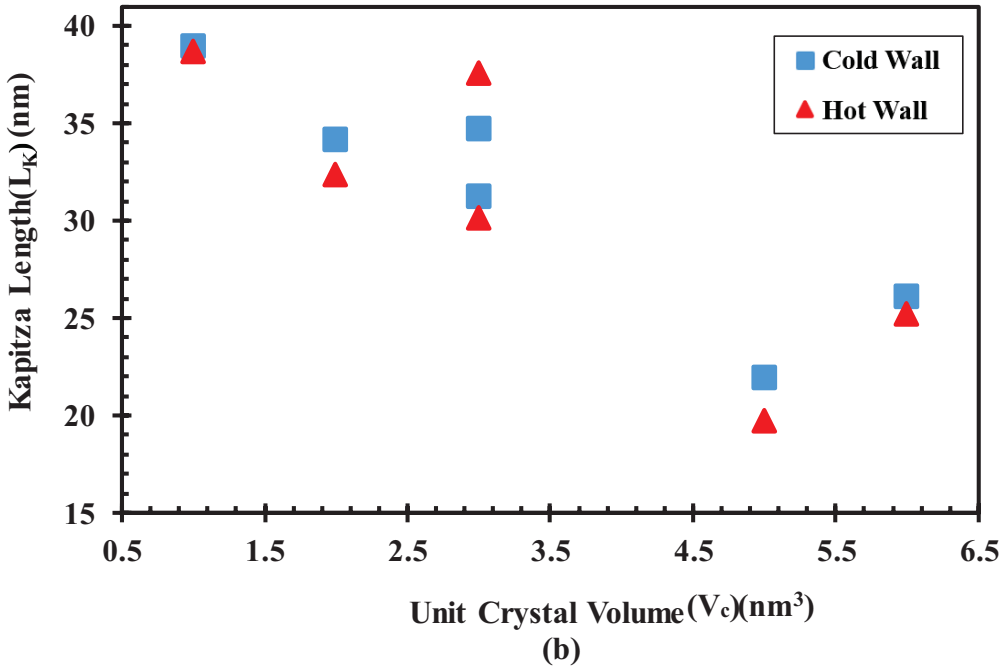

Figure 4.10. Average Kapitza Length values vs Unit Crystal Volume of 7 nanopatterned surface models for (a) ε=1.0 condition, and (b) ε=0.1 condition

Changing of Kapitza length with cavity width and cavity height for ε=1.0 and ε=0.1 condition is also studied in this thesis. As mentioned before, 7 nanopatterned structures have different notation due to their cavity height and cavity width. Since R11, R21, and R31 have the same cavity height but different cavity width, changing of Kapitza length with cavity width can be directly observed. As can be seen in Figure 3.5, the cavity height is represented as h while the cavity width is represented as w. The length of each w and h parameter is 5.063 Å. As an example, the R11 model has a 5.063 Å cavity width, and 5.063 Å cavity height. In the ε=1.0 condition, the changing of Kapitza length with channel cavity width can be seen in Figure 4.11a. Average Kapitza length values increased with the increase of cavity width. A similar approach is using to observe the effect of cavity height. Since R31, R32, and R33 have the same cavity width but different cavity height, changing average Kapitza length with respect to cavity height is observed in Figure 4.11b. However, the results are the opposite of other approaches. Average Kapitza length values decreased with the increase of channel cavity height. In general, the average Kapitza length increased by 7% when the channel cavity width increased. Also, average Kapitza length decreased by 17% when channel cavity height increased for ε=1.0 condition.

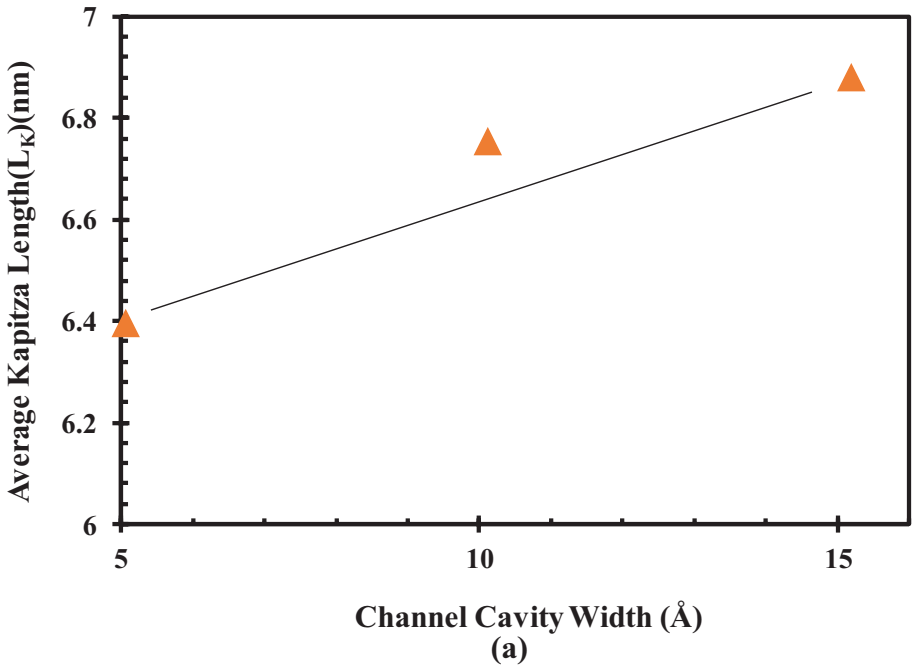

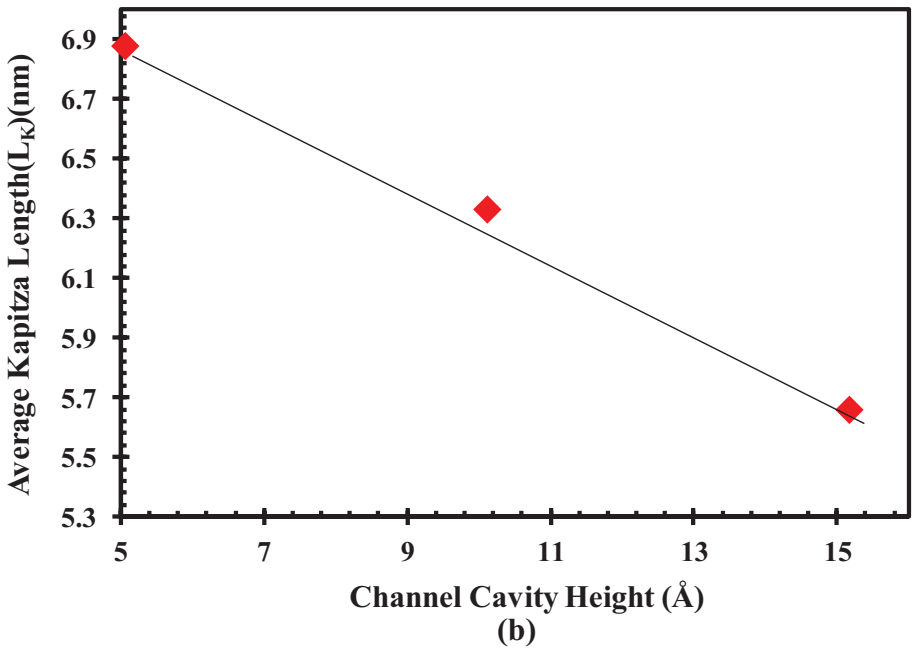

Figure 4.11. Changing average Kapitza length with respect to (a) Channel cavity width, (b) Channel cavity height for ε=1.0 condition.

In the ε=0.1 condition, the measured average Kapitza length value of the smooth pattern is 30.84 nm. Average Kapitza length values first decreased and then increased with the increase of channel cavity width. Changing of average Kapitza length with channel cavity width is represented in Figure 4.12a. Similar observations are found with the increase of channel cavity width. Average Kapitza length values decreased to channel cavity height equals 10.126 Å, and then increased to when channel cavity height equals 15.189 Å. Changing of average Kapitza length with channel cavity height is represented in Figure 4.12b. In general, the average Kapitza length decreased by approximately 7% when the channel cavity width increased. Also, the average Kapitza length decreased by approximately 29% when channel cavity height increased.

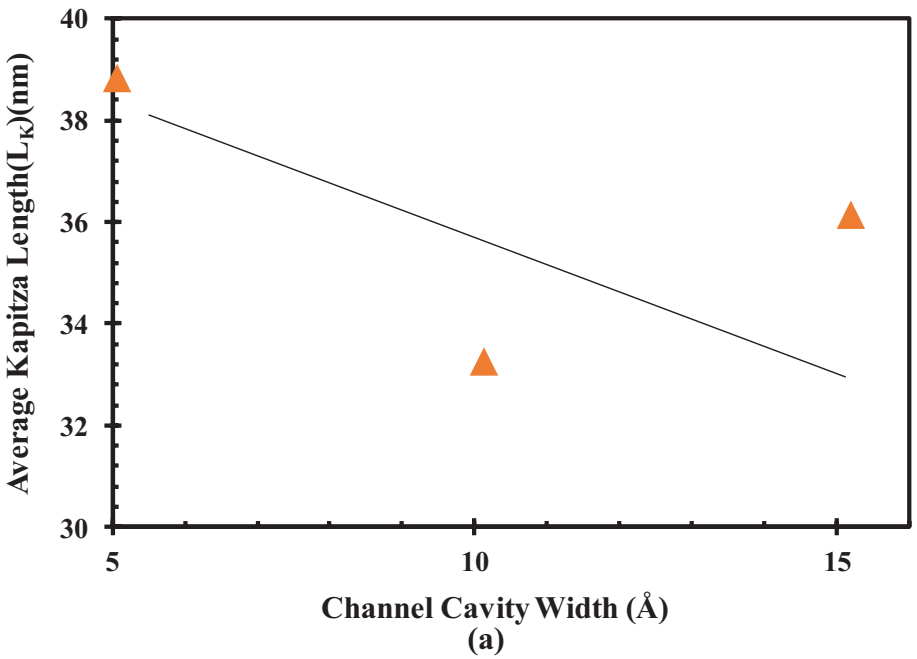

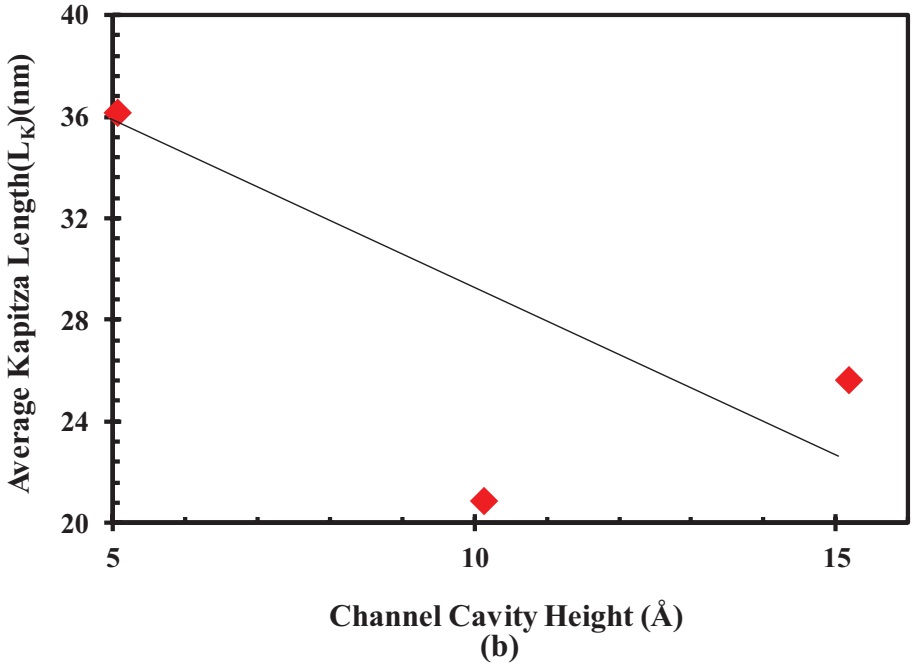

Figure 4.12. Changing average Kapitza length with respect to (a) Channel cavity width, (b) Channel cavity height for ε=0.1 condition.

To get rid of the complication that comes from the unit crystal volume explanation, another approach is used. In this approach, the number of removed V_c is

multiplied by the height of the cavity (h) and divided by the square of the width of the cavity (w), and a new parameter is obtained. This new parameter is denoted as A_c in this thesis. In addition, Figure 3.5 and 4.9 are used in this approach. Table 4.1 shows all parameters of A_c for other models.

Table 4.1. A_c parameters of different models.

Model	**A_c [$V_c h/w^2$ nm^2]**
R11	0.333333333
R21	0.5
R22	1
R31	1.111111111
R32	1.5
R33	2

After these parameters are obtained, the effect of Unit Crystal Volume*Height/Width of the Cavity^2 on Kapitza length is observed in Figure 4.13 for ε=1.0 and ε=0.1 conditions. The reason for this approach is the standardization of the cavity volume of the patterns. Unlike in Figure 4.10, average Kapitza length values at the cold and hot wall is calculated. In Figure 4.13 (a), the average Kapitza length decreased linearly when A_c increased for the ε=1.0 condition. In general, the average Kapitza length decreased by approximately 19% in the ε=1.0 condition. However, in Figure 4.13 (b), the average Kapitza length values behave differently. First, the average Kapitza length decreased. Then, it became maximum when A_c equals 1. Next, it decreased to the minimum value when A_c equals 1.11. After that, it increased until A_c equals 1.5. Finally, it decreased. . In general, the average Kapitza length decreased by approximately 29% in the ε=0.1 condition.

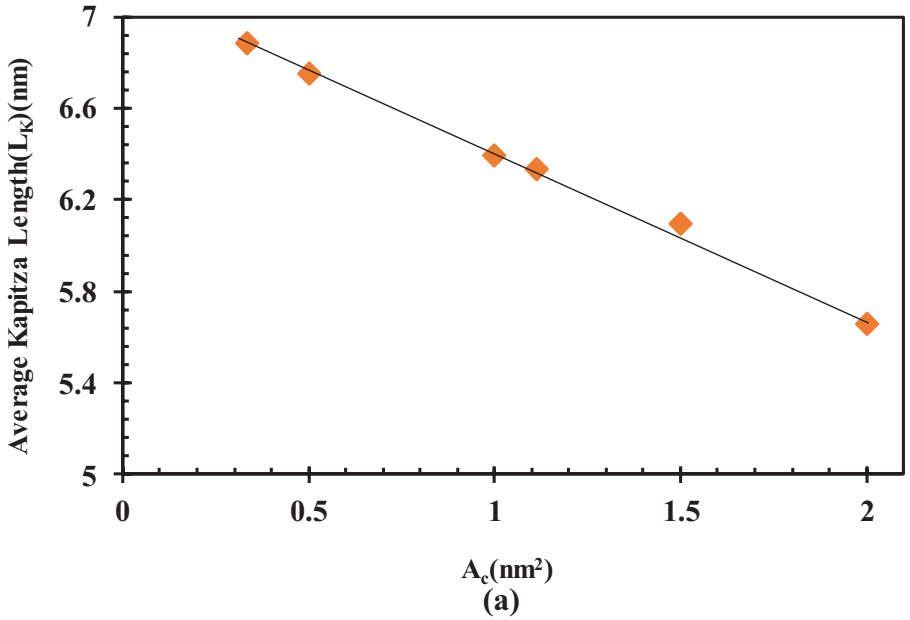

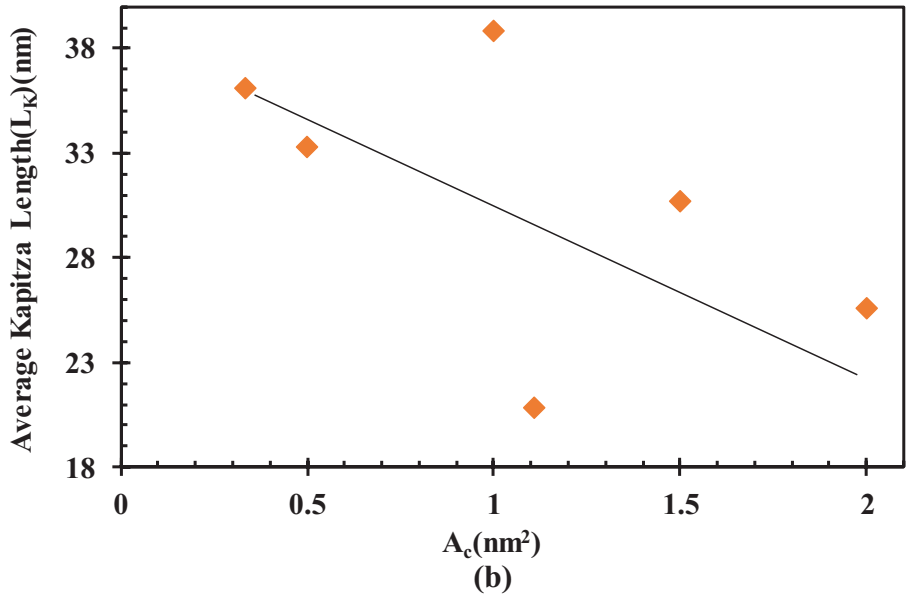

Figure 4.13. Average Kapitza Length values with respect to A_c of 7 nanopatterned surface models for (a) ε=1.0 condition, and (b) ε=0.1 condition.

After average Kapitza length values calculated for different conditions such as V_c, channel cavity width, channel cavity height, and A_c, average heat flux values are calculated for similar conditions using equation (3.8), (3.9), and (3.10). Using the LAMMPS script, heat flux values are calculated for different surface structures in x, y, and z directions. Since heat is transferred in the z-direction, heat flux values in this direction are used. After averaging heat flux values in the z-direction, the obtained value is divided by the volume of the model. Unit of the average heat flux values become eV/ps/

$Å^2$. To convert this unit to GW/m^2, the average heat flux value of the models is multiplied by $1.60217646x10^4$. According to general results, average heat flux values for the ε=1.0 condition is approximately 3 times greater than average heat flux values for the ε=0.1 condition. Also, the average heat flux of smooth pattern which is R00 is found as 2.52 GW/m^2, and 0.85 GW/m^2 for ε=1.0 and ε=0.1 conditions, respectively.

To check the accuracy of the results obtained, the thermal conductivity of water for ε=1.0 and ε=0.1 conditions are calculated based on the formula below:

$$q = k \frac{\partial T}{\partial n}\Big|_{liquid}, \tag{4.1}$$

where q is the heat flux, k is the water thermal conductivity, and $\partial T/\partial n$ is the temperature gradient of the water. Units of q, k, and $\partial T/\partial n$ are W/m^2, W/mK, and K/m, respectively. In the literature, the thermal conductivity of water in the SPC/E model is taken as 0.82 W/mK. However, MD gives thermal conductivity results a bit differently. So, the calculated thermal conductivity values must be close to 0.82 W/mK. Table 4.2 and 4.3 show the thermal conductivity of water for ε=1.0 and ε=0.1 conditions, respectively for each condition.

Table 4.2. Thermal conductivity of water for each model for high wetting condition

Model	Water Thermal Conductivity(W/mK)
R00	0.74
R11	0.75
R21	0.75
R22	0.79
R31	0.73
R32	0.78
R33	0.82

Table 4.3. Thermal conductivity of water for each model for low wetting condition

Model	Water Thermal Conductivity(W/mK)
R00	0.82
R11	0.82
R21	0.78
R22	0.83
R31	0.82
R32	0.75
R33	0.81

Firstly, the changing of average heat flux values with different numbers of V_c is observed in Figure 4.14 for ε=1.0 and ε=0.1 conditions. In the ε=1.0 condition which is shown in Figure 4.14a, the average heat flux value decreased until V_c equals 2 and then made a sudden increase when V_c equals 3. As mentioned before, R22 and R31 have the same crystal volume but different geometries. Because of this, average heat flux values differ. The average heat flux value of R31 is lower than R22 due to its roughness parameters. That's why there is a sudden decrease when V_c equals 3. After this point, the average heat flux increased. In total, average heat flux values are increased by approximately 5% in ε=1.0 condition. In ε=0.1 condition, general average heat flux values are approximately one-third of ε=1.0 condition and represented in Figure 4.14b. The average heat flux values increased when V_c equals 3 then made a sudden decrease again. After this sudden decrease, it increased until V_c become 5, then decreased. In general, average heat flux increased by approximately 17.2% when unit crystal volume increased.

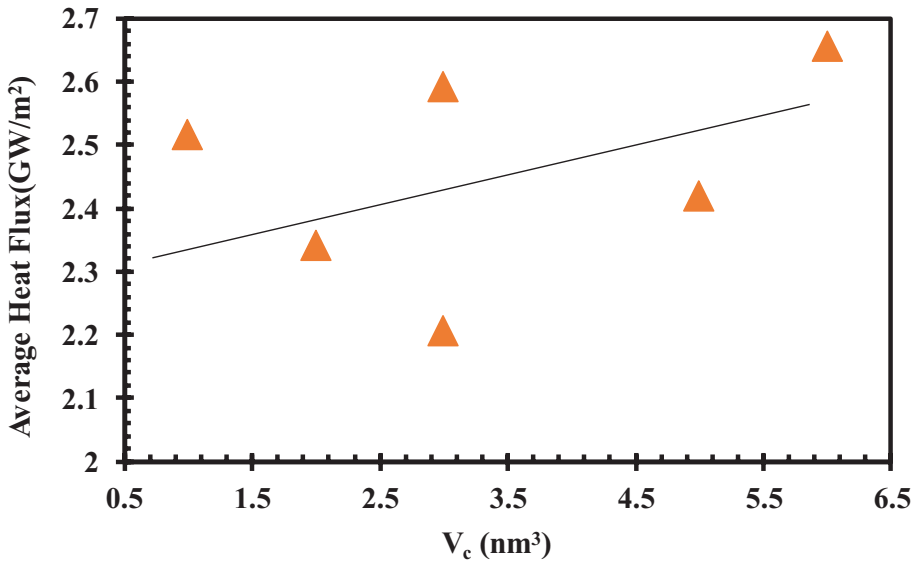

(a)

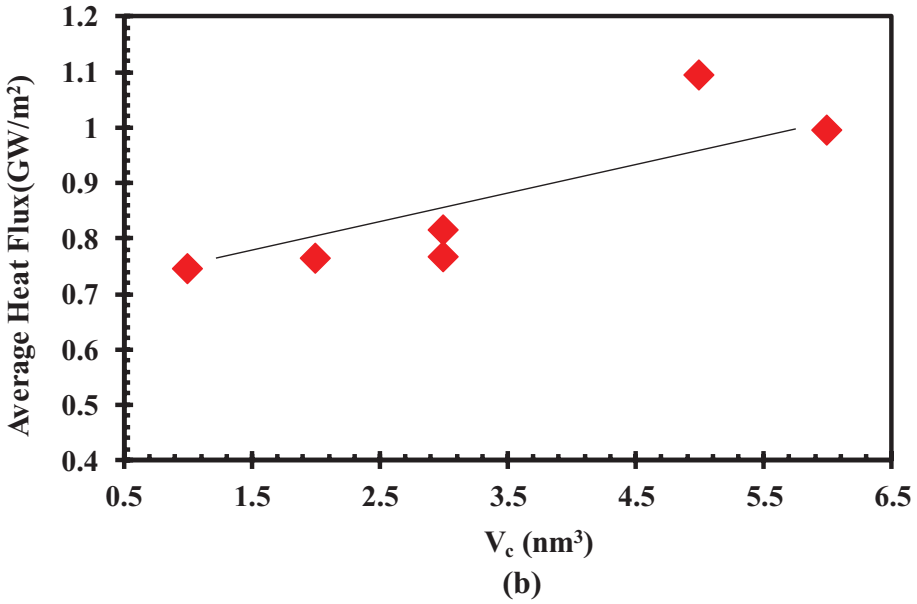

Figure 4.14. Changing of average heat flux with respect to unit crystal volume for (a) ε=1.0 condition, (b) ε=0.1 condition.

After the effect of V_c on average heat flux is observed, changing average heat flux with the channel cavity width and height achieved for ε=1.0 and ε=0.1 conditions which are shown in Figure 4.15. In the ε=1.0 condition, average heat flux decreased when the channel cavity width increased. The average heat flux decreased by approximately 12.6% in the ε=1.0 condition. Changing of average heat flux with channel cavity width for ε=1.0 and ε=0.1 conditions are represented in Figure 4.15a, 4.15b, respectively. However, in the ε=0.1 condition, the average heat flux slightly increased when the channel cavity width increased. In general, average heat flux increased by 2.8% in the ε=0.1 condition. Next, the changing of average heat flux with respect to channel cavity height is investigated in Figure 4.16a for ε=1.0 condition, and Figure 4.16b for ε=0.1 condition. In the ε=1.0 condition, the average heat flux increased when channel cavity height increased. In general, the average heat flux increased by approximately 20% in the ε=1.0 condition. In the ε=0.1 condition, the average heat flux increased until channel cavity height equals 10.126 Å, and then decreased. As a result, the average heat flux increased by approximately 30% in the ε=0.1 condition.

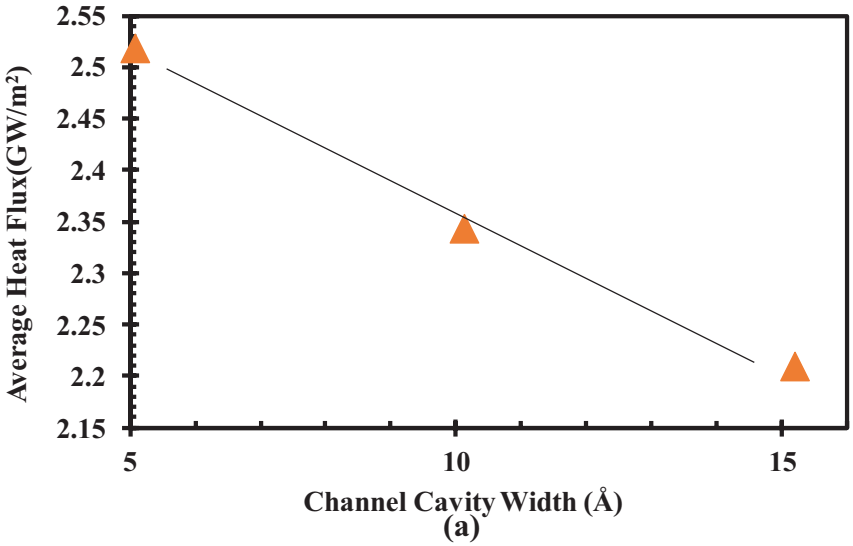

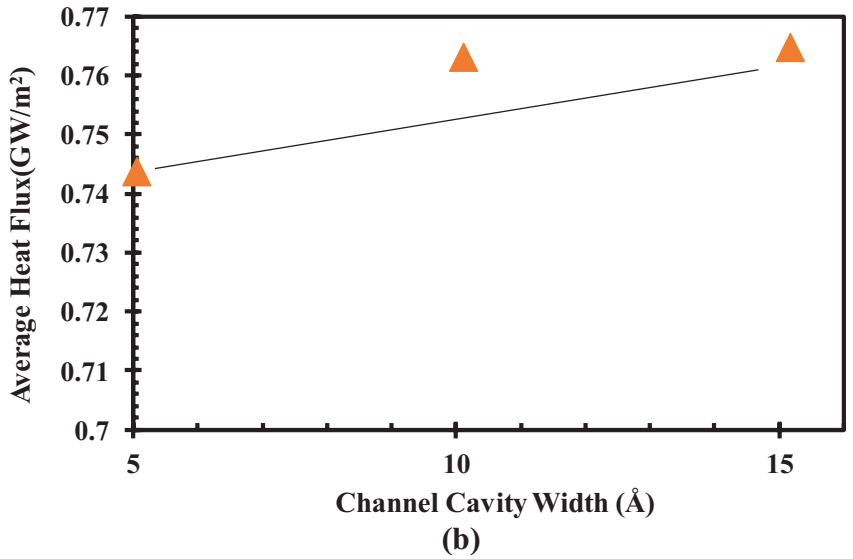

Figure 4.15. Changing average heat flux with channel cavity width for (a) ε=1.0 condition, (b) ε=0.1 condition.

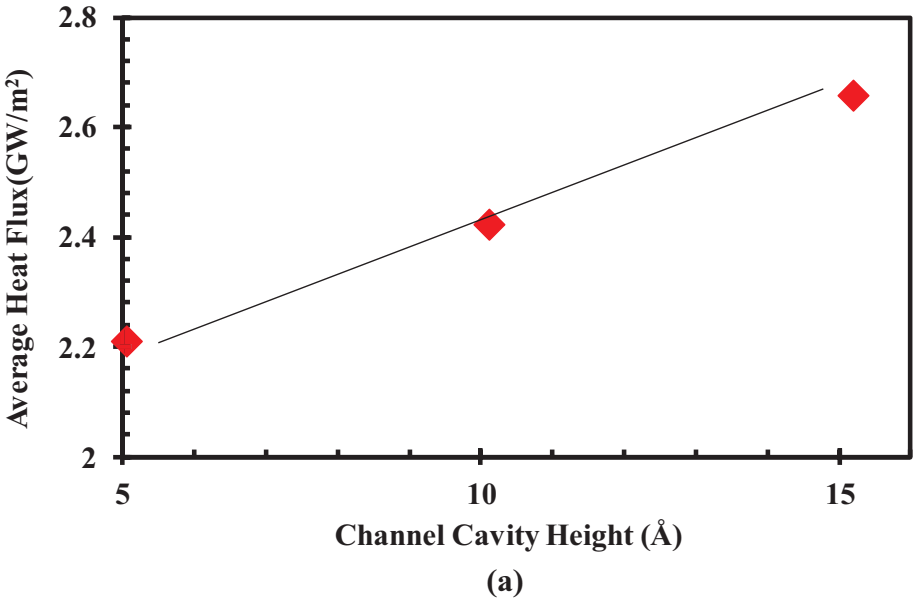

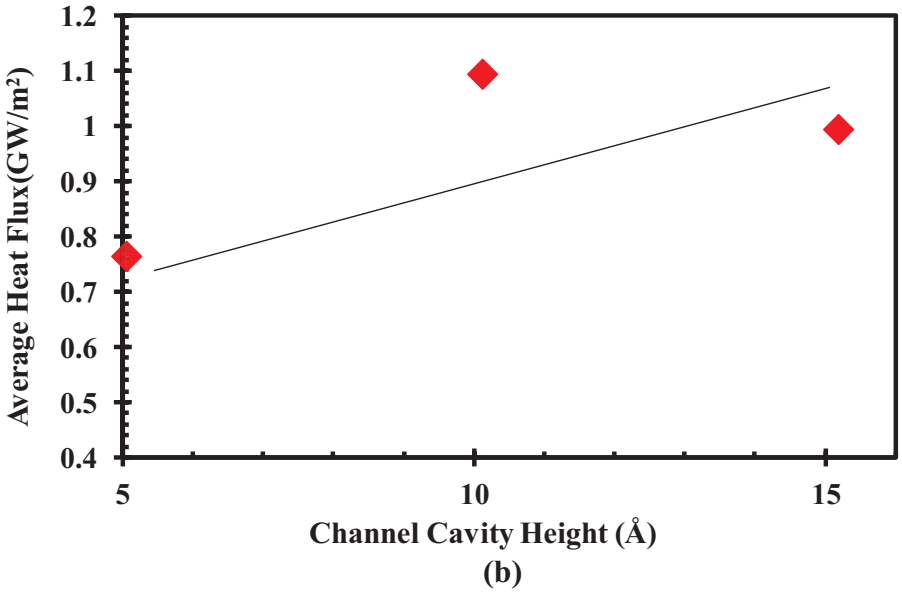

Figure 4.16. Changing average heat flux with channel cavity height for (a) ε=1.0 condition, (b) ε=0.1 condition.

The final approach is changing average heat flux with A_c for ε=1.0, and ε=0.1 conditions which are represented in Figure 4.17a, and Figure 4.17b, respectively. In the ε=1.0 condition, the average heat flux increased until A_c equals 1. After this point, it decreased until A_c equals 1.1 and then increased. In general, the average heat flux increased by 20% when A_c increased. In the ε=0.1 condition, the average heat flux

decreased until A_c equals 1. After, it increased until A_c is 1.1, then decreased until A_c equals 1.5. Finally, it increased until A_c equals 2. In general, the average heat flux is increased by approximately 30% in ε=0.1 condition.

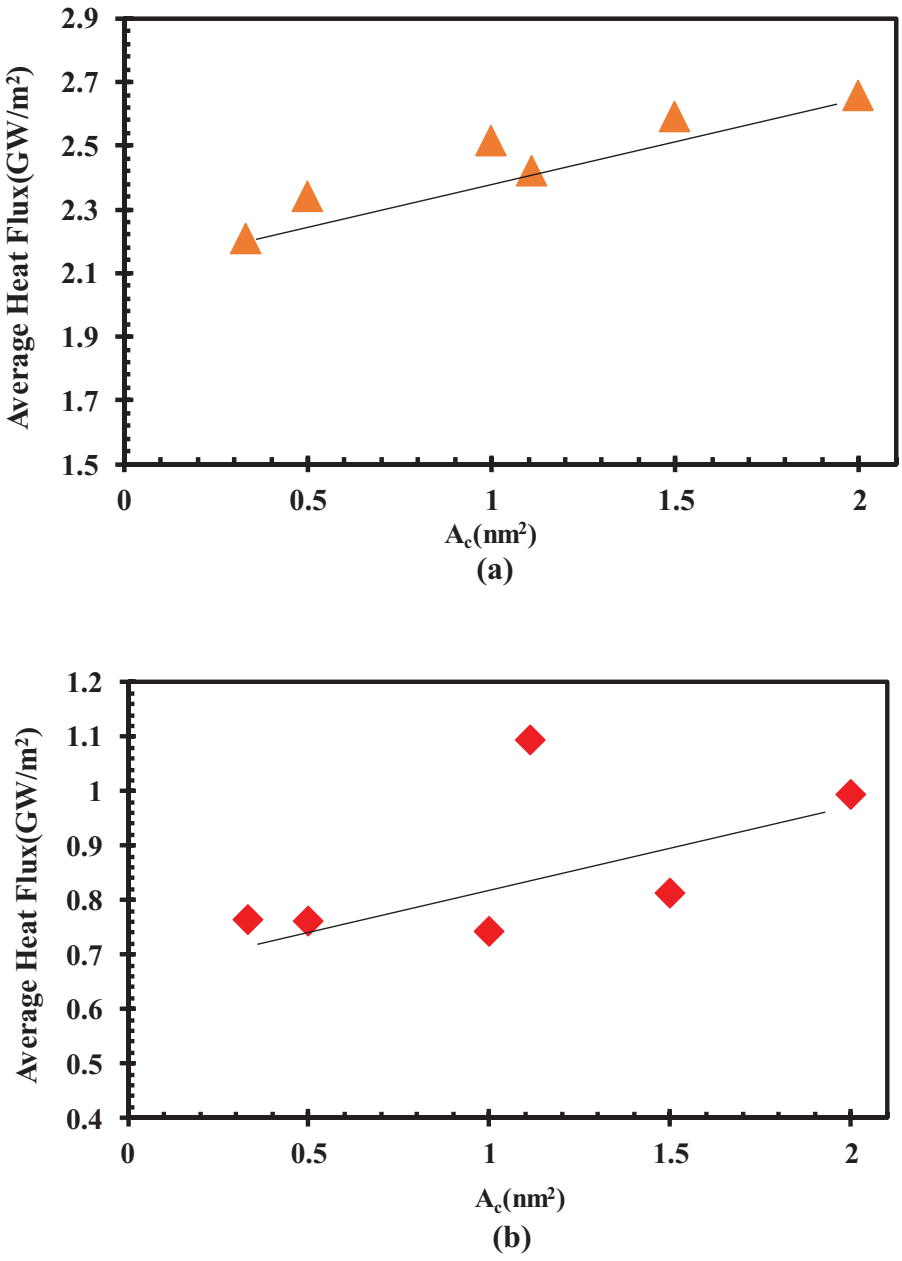

Figure 4.17. Changing average heat flux with A_c for (a) ε=1.0 condition, (b) ε=0.1 condition.

Also, changing normalized heat flux with respect to A_c is studied. All average heat flux values are divided by the heat flux at A_c=0.3333. The reason for this is obtaining a clear indication of the increase or decrease in average heat flux values. Figure 4.18a and 4.18b

show the changing normalized heat flux with the increase of A_c. As mentioned before, normalized heat flux increased by 20% and 30% for ε=1.0 and ε=0.1 conditions, respectively, when A_c increased.

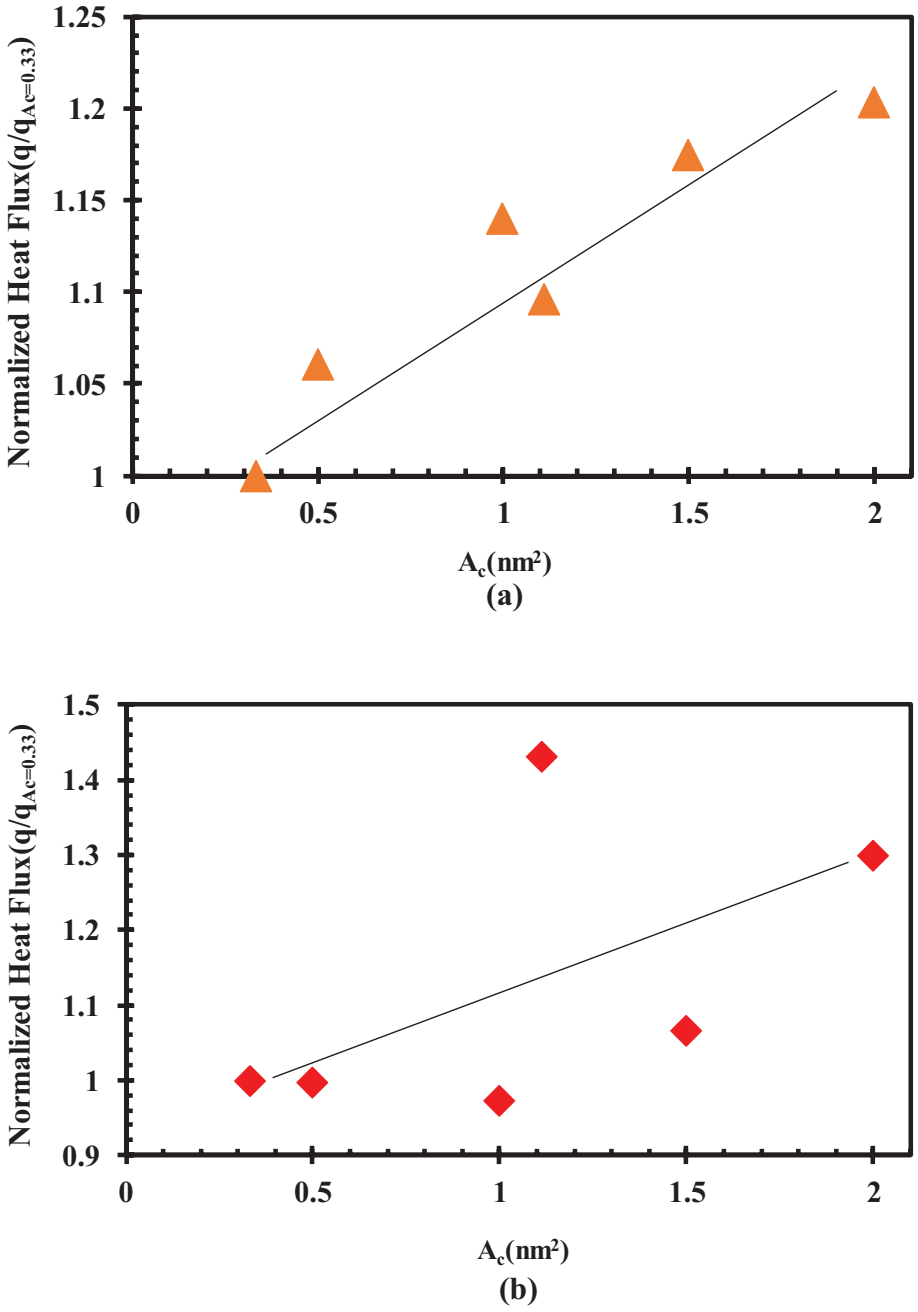

Figure 4.18. Changing normalized heat flux with A_c for (a) ε=1.0 condition, (b) ε=0.1 condition.

CHAPTER 5

CONCLUSION

Device sizes have shrunk in the last 20 years due to advances in technologies in the computer electronics, communication, and manufacturing fields. The operating rate and memory of these devices increased. However, thermal management problems have occurred. To overcome thermal management problems, a new field of study is called nanoscale heat transfer appeared. In this thesis, nanoscale heat transfer is observed as interfacial thermal resistance or Kapitza length at the solid-liquid interface. Kapitza length is one of the important phenomena when defining heat transfer in nanoscale. Also, the effect of the surface patterns with different geometry on heat transfer is observed. Along with these observations, the effect of interatomic strength between atoms on Kapitza length is also observed for two different conditions.

An effective and time efficient way to investigate heat transfer in nanoscale is MD simulations. Molecular dynamics simulations are deal with the physical movements of atoms and molecules. In this thesis, developing the main surface structure or called a smooth pattern was the first step to investigate heat transfer at the interface. Two parallel silica walls containing water molecules between them were modeled. In the modelling part, molecular interactions such as are Lennard-Jones and Coulombic potentials used. Lorentz-Berthelot mixing rule was used to calculate molecular interaction between dissimilar atoms such as silicon-oxygen. However, the precision of the LB rule was not satisfied with silicon and oxygen interaction. Instead of this, the molecular interaction between silicon-oxygen that is obtained by Barisik and Beskok was used. As mentioned before, two different molecular interaction strength parameters were used. In ε=1.0 or called the high wetting condition, molecular interaction strength values between H-H, O-O, and Si-O are 0, 0.006739, and 0.01511, respectively. In ε=0.1 or called the low wetting condition, molecular interaction strength values between H-H, O-O, and Si-O are 0, 0.0006739, and 0.001511, respectively. For water modelling, the SPC/E water model and SHAKE algorithm were applied. Beta-cristobalite form of silica was preferred due to its high temperature.

After obtaining water models, silica models, and molecular interactions, the surface pattern of the smooth model was manipulated to investigate heat transfer on different surface patterns. Seven different nanopatterned surface structures were created in total. Each model has a different unit crystal cavity volume and is denoted as R00, R11, R21, R22, R31, R32, and R33. Then, the LAMMPS script was used as an MD solver. NVT ensemble was used for 7 nanoscale surface structures to obtain thermodynamically stable simulation at 323 K. Then NVE ensemble was used to create heat transfer across the model between 283 K and 363 K. Finally, Verlet time algorithm was applied for these parameters.

The simulation domain is containing three different regions: Cold reservoir, water region, and hot reservoir. The temperature and density results of MD simulations in every location were obtained by using the LAMMPS script. Results and discussion part which is Chapter 4 is starting with one-dimensional density profiles for ε=1.0, and ε=0.1 conditions. The reason for this to compare simulation density data of water and silicon with theoretical values. 7 nanopatterned surface structures had different behavior and the wall locations of 7 models were different according to results. Also, two-dimensional density distribution was obtained and represented with different color saturation. After that, needed parameters were obtained to calculate Kapitza length at the silica-water interface. Firstly, the two-dimensional temperature distribution was obtained to investigate each region of the model. Then, one-dimensional temperature profiles of 7 models were created for ε=1.0, and ε=0.1 conditions or called high wetting and low wetting conditions. The temperature gradient of water for the high wetting condition was approximately four times greater than the low wetting condition. However, temperature jumps at the cold wall and the hot wall was greater in ε=0.1 by 10 K. To analyze the behavior of surface structures detailly, one-dimensional temperature profiles of R11 and R33 for ε=1.0 and ε=0.1 condition were obtained. In the LAMMPS script, y and z directions were divided by 12 and 300 slabs, respectively. In the ε=1.0 condition, the deepest locations of the cavity have the highest temperature jump values. If R11 and R33 are compared to each other, the temperature jumps of the cold and hot reservoirs decreased in R33. In the ε=1.0 condition, temperature jumps decreased in the R33 model. However, they are much higher than the R33 model for the ε=1.0 condition. Also, the average water temperature gradient of the R33 model is greater than the R11 model for ε=0.1 condition. Since y-direction has 12 slabs or called layers, 12 Kapitza length values

are calculated for 7 different nanopatterned surface structures for ε=1.0, and ε=0.1 condition. In the ε=1.0 condition, $L_{K\text{-}COLD}$ is greater than $L_{K\text{-}HOT}$ except for R32 and R33 patterns. Also, Kapitza length of the top layers is greater than wKapitza length of the cavity section. The deepest locations of the cavities have the lowest Kapitza length values. In the ε=0.1 condition, $L_{K\text{-}COLD}$ is greater than $L_{K\text{-}HOT}$ except for the R31 pattern. Also, $L_{K\text{-}COLD}$ and $L_{K\text{-}HOT}$ values for the cavity section are greater than the top layers in R31 and R32 patterns. Also, the deepest points of the cavity have the highest $L_{K\text{-}COLD}$ values in the R32 pattern.

Although these Kapitza length calculations were obtained, the effect of cavity volume on Kapitza length cannot be investigated detailly. To overcome this, the unit crystal cavity volume parameter was defined and denoted as V_c. The number of removed unit crystal cavity volume of R11, R21, R22, R31, R32, and R33 are 1, 2, 3, 3, 5, and 6, respectively. Averaging 12 Kapitza length values for cold and hot wall with respect to unit crystal cavity volume was represented for ε=1.0 and ε=0.1 conditions in Chapter-4. However, the results were not clear since R22 and R31 have the same removed V_c. In other words, a general characterization of cavity volume could not be obtained. To overcome this problem, Unit Crystal Cavity Volume*Cavity Height/Width of Cavity^2 parameter of each model is defined and denoted as A_c and represented in Table 4.1. Average of average Kapitza length values of hot and cold walls with respect to A_c was obtained. Kapitza length values of ε=1.0 condition were much lower than ε=0.1 condition. The reason for this, weaker H-H, O-O, and Si-O interactions caused a lower water temperature gradient and higher temperature jumps. So, Kapitza length increased in ε=0.1 condition. Also, the average Kapitza length decreased linearly when A_c increased for the ε=1.0 condition. However, it behaved differently for the ε=0.1 condition. The average Kapitza length decreased by approximately 19% and 29% for ε=1.0 condition and ε=0.1 condition, respectively, when A_c increased.

Finally, changing average heat flux with V_c, channel width, channel height, and A_c are observed. To check the accuracy of results, the water thermal conductivity of each model is calculated for high and low wetting conditions. According to water thermal conductivity values, our results are valid. Results showed that the average heat flux of the ε=1.0 condition is approximately three times greater than the ε=0.1 condition. Overall, the average heat flux increased by approximately 20% and 30% for ε=1.0 and ε=0.1 conditions, respectively, when A_c increased.

REFERENCES

(1) Wu, A. R.; Yu, L. There's Plenty of Room at the Bottom of a Cell. *Chem. Eng. Prog.* **2017**, *113* (10).

(2) Darabi, J. Editorial: Micro- and Nanoscale Heat Transfer: Challenges and Opportunities. *Heat Transf. Eng.* **2002**, *23* (2), 1–2.

(3) O'Sullivan, C. T. Newton's Law of Cooling—A Critical Assessment. *Am. J. Phys.* **1990**, *58* (10), 956–960.

(4) Liu, I. S. On Fourier's Law of Heat Conduction. *Contin. Mech. Thermodyn.* **1990**, *2* (4), 301–305.

(5) Luo, T.; Chen, G. Nanoscale Heat Transfer-from Computation to Experiment. *Phys. Chem. Chem. Phys.* **2013**, *15* (10), 3389–3412.

(6) Cahill, D. G.; Ford, W. K.; Goodson, K. E.; Mahan, G. D.; Majumdar, A.; Maris, H. J.; Merlin, R.; Phillpot, S. R. Nanoscale Thermal Transport. *J. Appl. Phys.* **2003**, *93* (2), 793–818.

(7) Papavassiliou, D. V. Understanding Macroscopic Heat/Mass Transfer Using Meso- and Macro-Scale Simulations. *Model Reduct. Coarse-Graining Approaches Multiscale Phenom.* **2006**, 489–513.

(8) Cahill, D. G.; Braun, P. V.; Chen, G.; Clarke, D. R.; Fan, S.; Goodson, K. E.; Keblinski, P.; King, W. P.; Mahan, G. D.; Majumdar, A.; Maris, H. J.; Phillpot, S. R.; Pop, E.; Shi, L. Nanoscale Thermal Transport. II. 2003-2012. *Appl. Phys. Rev.* **2014**, *1* (1).

(9) Rogers, B.; Adams, J.; Pennathur, S. Nanoscale Heat Transfer. *Nanotechnology*. 2013, pp 219–236.

(10) Luckyanova, M. N.; Mendoza, J.; Lu, H.; Song, B.; Huang, S.; Zhou, J.; Li, M.; Dong, Y.; Zhou, H.; Garlow, J.; Wu, L.; Kirby, B. J.; Grutter, A. J.; Puretzky, A. A.; Zhu, Y.; Dresselhaus, M. S.; Gossard, A.; Chen, G. Phonon Localization in Heat Conduction. *Sci. Adv.* **2018**, *4* (12), 1–28.

(11) Shinde, S. L.; Piekos, E. S.; Sullivan, J. P.; Friedmann, T. A.; Hurley, H.; Aubry, S.; Peebles, D. E.; Emerson, J. A. Phonon Engineering for Nanostructures. *Structure* **2010**, No. January.

(12) Villela, lucia maria aversa. Phonon-Phonon Interaction in Crystals. *J. Chem. Inf. Model.* **2013**, *53* (9), 1689–1699.

(13) Bayati, N.; Hajizadeh, A.; Soltani, M. ReView by River Valley This Technologies Protection in DC Microgrids : A Comparative Review IET Review Copy Only ReView by River Valley This Technologies Article Has Been Accepted for Publication in a Future Issue of This Journal , but Has Not Been Fully . **2018**, 2–15.

(14) Hatanaka, D.; Mahboob, I.; Onomitsu, K.; Yamaguchi, H. Phonon Waveguides for Electromechanical Circuits. *Nat. Nanotechnol.* **2014**, *9* (7), 520–524.

(15) Kryder, M. H.; Gage, E. C.; Mcdaniel, T. W.; Challener, W. A.; Rottmayer, R. E.; Ju, G.; Hsia, Y. T.; Erden, M. F. Heat Assisted Magnetic Recording. *Proc. IEEE* **2008**, *96* (11), 1810–1835.

(16) Radhakrishnan, R.; Vasić, B.; Erden, F.; He, C. Characterization of Heat-Assisted Magnetic Recording Channels. **2008**, *73* (70), 23–39.

(17) Vogler, C.; Abert, C.; Bruckner, F.; Suess, D.; Praetorius, D. Heat-Assisted Magnetic Recording of Bit-Patterned Media beyond 10 Tb/In2. *Appl. Phys. Lett.* **2016**, *108* (10), 1–5.

(18) Seagate. HAMR Technology Paper. **2017**.

(19) Sen, T.; Barisik, M. Size Dependent Surface Charge Properties of Silica Nano-Channels: Double Layer Overlap and Inlet/Outlet Effects. *Phys. Chem. Chem. Phys.* **2018**, *20* (24), 16719–16728.

(20) Hu, H.; Xu, C.; Zhao, Y.; Ziegler, K. J.; Chung, J. N. Boiling and Quenching Heat Transfer Advancement by Nanoscale Surface Modification. *Sci. Rep.* **2017**, *7* (1), 1–16.

(21) Rapaport, D. C. An Introduction to Molecular Dynamics Simulation. *Comput. Simulations Surfaces Interfaces* **2003**, *23*, 59–73.

(22) Geysermans, P.; Gorse, D.; Pontikis, V. Molecular Dynamics Study of the Solid-Liquid Interface. *J. Chem. Phys.* **2000**, *113* (15), 6382–6389.

(23) Barrat, J.; Chiaruttini, F. Kapitza Resistance at the Liquid—Solid Interface. *Mol. Phys.* **2003**, *101* (11), 1605–1610.

(24) Shi, L.; Dames, C.; Lukes, J. R.; Reddy, P.; Duda, J.; Cahill, D. G.; Lee, J.; Marconnet, A.; Goodson, K. E.; Bahk, J. H.; Shakouri, A.; Prasher, R. S.; Felts, J.; King, W. P.; Han, B.; Bischof, J. C. Evaluating Broader Impacts of Nanoscale Thermal Transport Research. *Nanoscale Microscale Thermophys. Eng.* **2015**, *19* (2), 127–165.

(25) Shapiro, I. M. Chapter 7 Cooling and Integrated Heating / Cooling Systems. **2020**, No. or DX, 117–135.

(26) Ruch, P.; Ammann, J.; Paredes, S.; Wiik, N.; Lörtscher, E.; Meijer, G. I.; Michel, B. Sustainable Data Centers and Energy Conversion Technologies. *Proc. 12th IEA Heat Pump Conf.* **2017**, *2*, 1–8.

(27) Chen, G. Thermoelectric Energy Conversion: Materials, Devices, and Systems. *J. Phys. Conf. Ser.* **2015**, *660* (1).

(28) Turcato, D. Saving the Future. *Anarch. 1914–18* **2018**.

(29) Sun, Y.; Agostini, N. B.; Dong, S.; Kaeli, D. Summarizing CPU and GPU Design Trends with Product Data. *arXiv* **2019**.

(30) Nakayama, W. Heat in Computers: Applied Heat Transfer in Information Technology. *J. Heat Transfer* **2014**, *136* (1).

(31) Horiguchi, N.; Parvais, B.; Chiarella, T.; Collaert, N.; Veloso, A.; Rooyackers, R.; Verheyen, P.; Witters, L.; Redolfi, A.; De Keersgieter, A.; Brus, S.; Zschaetzsch, G.; Ercken, M.; Altamirano, E.; Locorotondo, S.; Demand, M.; Jurczak, M.; Vandervorst, W.; Hoffmann, T.; Biesemans, S. FinFETs and Their Futures. **2011**, No. February, 141–153.

(32) In, C.; Nitride, G.; Substrates, C. Annual Review of Heat Transfer , Invited and Submitted Annual Review of Heat Transfer , Invited and Submitted. 1–65.

(33) Atta, R. M. Thermoelectric Cooling (Chpater 12). **2018**, 247–267.

(34) Ghodake, D.; Kashid, D. Design and Performance Analysis of Heat Exchanger for Thermoelectric Power Generation Using Exhaust Waste-Heat Energy. **2018**, No. July, 138–145.

(35) Torres-Martínez, L. M.; Kharissova, O. V.; Kharisov, B. I. Handbook of Ecomaterials. *Handb. Ecomater.* **2019**, *1* (February), 1–3773.

(36) Nadeau, J. L. Introduction to Experimental Biophysics: Biological Methods for Physical Scientists. *Introd. to Exp. Biophys.* **2018**, No. December.

(37) Sobhan, C. B.; Thomas, S.; Peterson, G. P. Microscale Transport Phenomena for Bio-Engineering Applications: Recent Advances. *J. Adv. Nanomater.* **2017**, No. March.

(38) Bui, H.; Shah, S.; Mokhtar, R.; Song, T.; Garg, S.; Reif, J. Localized DNA Hybridization Chain Reactions on DNA Origami. *ACS Nano* **2018**, *12* (2), 1146–1155.

(39) Chilukoti, H. K.; Kikugawa, G.; Shibahara, M.; Ohara, T. Local Thermal Transport of Liquid Alkanes in the Vicinity of α-Quartz Solid Surfaces and Thermal Resistance over the Interfaces: A Molecular Dynamics Study. *Phys. Rev. E - Stat. Nonlinear, Soft Matter Phys.* **2015**, *91* (5).

(40) Amrit, J.; Ramiere, A. Kapitza Resistance between Superfluid Helium and Solid: Role of the Boundary. *Low Temp. Phys.* **2013**, *39* (9).

(41) Budaev, B. V.; Bogy, D. B. An Extension of Khalatnikov's Theory of Kapitsa Thermal Resistance. *Ann. der Phys.* **2011**, *523* (3), 208–225.

(42) Davidzon, M. Y. About Navier-Stokes Equation in the Theory of Convective Heat Transfer. *J. Phys. Conf. Ser.* **2017**, *891* (1).

(43) Sahraoui, M.; Kaviany, M. Slip and No-Slip Temperature Boundary Conditions at the Interface of Porous, Plain Media: Convection. *Int. J. Heat Mass Transf.* **1994**, *37* (6), 1029–1044.

(44) Kim, B. H.; Beskok, A.; Cagin, T. Thermal Interactions in Nanoscale Fluid Flow: Molecular Dynamics Simulations with Solid-Liquid Interfaces. *Microfluid. Nanofluidics* **2008**, *5* (4), 551–559.

(45) Sun, J.; Wang, W.; Wang, H. S. Dependence between Velocity Slip and Temperature Jump in Shear Flows. *J. Chem. Phys.* **2013**, *138* (23).

(46) De Bellis, L.; Phelan, P. E.; Prasher, R. S. Variations of Acoustic and Diffuse Mismatch Models in Predicting Thermal-Boundary Resistance. *J. Thermophys. heat Transf.* **2000**, *14* (2), 144–150.

(47) Ma, D.; Zhang, Y.; Zang, Y.; Yang, N. A Modified Theoretical Model to Predict the Thermal Interface Conductance Considering Interface Roughness. *Int. Heat Transf. Conf.* **2018**, *2018-Augus*, 6029–6035.

(48) Khvesyuk, V. I.; Liu, B.; Barinov, A. A. Development of Acoustic and Diffuse Mismatch Models for Predicting the Kapitza Resistance. *J. Phys. Conf. Ser.* **2019**, *1382* (1).

(49) Khvesyuk, V. I.; Liu, B.; Barinov, A. A. A New Look at Kapitza Conductance Calculation (Thermal Boundary Resistance). *J. Phys. Conf. Ser.* **2019**, *1368* (4).

(50) Balasubramanian, G.; Banerjee, S.; Puri, I. K. Paper No . IMECE2008-69152. **2017**, 1–5.

(51) Pham, A. T.; Barisik, M.; Kim, B. Molecular Dynamics Simulations of Kapitza Length for Argon-Silicon and Water-Silicon Interfaces. *Int. J. Precis. Eng. Manuf.*

2014, *15* (2), 323–329.

(52) Kim, B. H.; Beskok, A.; Cagin, T. Molecular Dynamics Simulations of Thermal Resistance at the Liquid-Solid Interface. *J. Chem. Phys.* **2008**, *129* (17).

(53) Barisik, M.; Beskok, A. Temperature Dependence of Thermal Resistance at the Water/Silicon Interface. *Int. J. Therm. Sci.* **2014**, *77*, 47–54.

(54) Yenigun, O.; Barisik, M. Effect of Nano-Film Thickness on Thermal Resistance at Water/Silicon Interface. *Int. J. Heat Mass Transf.* **2019**, *134*, 634–640.

(55) Kalyoncu, G.; Barisik, M. Analytical Solution of Micro-/Nanoscale Convective Liquid Flows in Tubes and Slits. *Microfluid. Nanofluidics* **2017**, *21* (9).

(56) Roy, P.; Anand, N. K.; Banerjee, D. Liquid Slip and Heat Transfer in Rotating Rectangular Microchannels. *Int. J. Heat Mass Transf.* **2013**, *62* (1), 184–199.

(57) Sun, J.; Wang, W.; Wang, H. S. Dependence between Velocity Slip and Temperature Jump in Shear Flows. *J. Chem. Phys.* **2013**, *138* (23).

(58) Hong, Y.; Li, L.; Zeng, X. C.; Zhang, J. Tuning Thermal Contact Conductance at Graphene-Copper Interface via Surface Nanoengineering. *Nanoscale* **2015**, *7* (14), 6286–6294.

(59) Wang, Y.; Keblinski, P. Role of Wetting and Nanoscale Roughness on Thermal Conductance at Liquid-Solid Interface. *Appl. Phys. Lett.* **2011**, *99* (7), 2011–2014.

(60) Zhou, X. W.; Jones, R. E.; Kimmer, C. J.; Duda, J. C.; Hopkins, P. E. Relationship of Thermal Boundary Conductance to Structure from an Analytical Model plus Molecular Dynamics Simulations. *Phys. Rev. B - Condens. Matter Mater. Phys.* **2013**, *87* (9), 21–27.

(61) Remacle, J.; Lambrechts, J.; Seny, B. Blossom-Quad: A Non-uniform Quadrilateral Mesh Generator Using a Minimum-cost Perfect-matching Algorithm. *International* **2012**, No. February, 1102–1119.

(62) Sun, J.; He, Y. L.; Tao, W. Q.; Rose, J. W.; Wang, H. S. Multi-Scale Study of Liquid Flow in Micro/Nanochannels: Effects of Surface Wettability and Topology. *Microfluid. Nanofluidics* **2012**, *12* (6), 991–1008.

(63) Alder, B. J.; Wainwright, T. E. Phase Transition for a Hard Sphere System. *J. Chem. Phys.* **1957**, *27* (5), 1208–1209.

(64) Rossky, P. J. Perspective on "Correlations in the Motion of Atoms in Liquid Argon." *Theor. Chem. Acc.* **2000**, *103* (3–4), 263–264.

(65) Poulikakos, D.; Arcidiacono, S.; Maruyama, S. Molecular Dynamics Simulation

in Nanoscale Heat Transfer: A Review. *Microscale Thermophys. Eng.* **2003**, *7* (3), 181–206.

(66) Nijmeijer, M. J. P.; Bakker, A. F.; Bruin, C.; Sikkenk, J. H. A Molecular Dynamics Simulation of the Lennard-Jones Liquid-Vapor Interface. *J. Chem. Phys.* **1988**, *89* (6), 3789–3792.

(67) Ohara, T. Molecular Dynamics Study in Microscale Thermophysical Engineering: Current Activities and Future in Japan. *Microscale Thermophys. Eng.* **2000**, *4* (4), 213–221.

(68) Stoddard, S. D.; Ford, J. Experiments Stochastic Lennard-Jones. **1973**, *8* (3).

(69) van Zwol, P.; Joulain, K.; Ben Abdallah, P.; Greffet, J.; Chevrier, J. Fast Heat Flux Modulation at the Nanoscale. *eprint arXiv:1104.2994* **2011**.

(70) KATAOKA, Y.; YAMADA, Y. An Extended van Der Waals Equation of State Based on Molecular Dynamics Simulation. *J. Comput. Chem. Japan* **2009**, *8* (3), 97–104.

(71) Surblys, D.; Leroy, F.; Yamaguchi, Y.; Müller-Plathe, F. Molecular Dynamics Analysis of the Influence of Coulomb and van Der Waals Interactions on the Work of Adhesion at the Solid-Liquid Interface. *J. Chem. Phys.* **2018**, *148* (13), 1–3.

(72) Delhommelle, J.; Millié, P. Inadequacy of the Lorentz-Berthelot Combining Rules for Accurate Predictions of Equilibrium Properties by Molecular Simulation. *Mol. Phys.* **2001**, *99* (8), 619–625.

(73) Yang, J. Z.; Wu, X.; Li, X. A Generalized Irving-Kirkwood Formula for the Calculation of Stress in Molecular Dynamics Models. *J. Chem. Phys.* **2012**, *137* (13).

(74) Jorgensen, W. L.; Chandrasekhar, J.; Madura, J. D.; Impey, R. W.; Klein, M. L. Comparison of Simple Potential Functions for Simulating Liquid Water. *J. Chem. Phys.* **1983**, *79* (2), 926–935.

(75) Berendsen, H. J. C.; Grigera, J. R.; Straatsma, T. P. The Missing Term in Effective Pair Potentials. *J. Phys. Chem.* **1987**, *91* (24), 6269–6271.

(76) Van Der Spoel, D.; Van Maaren, P. J.; Berendsen, H. J. C. A Systematic Study of Water Models for Molecular Simulation: Derivation of Water Models Optimized for Use with a Reaction Field. *J. Chem. Phys.* **1998**, *108* (24), 10220–10230.

(77) Miyamoto, S.; Kollman, P. A. Settle: An Analytical Version of the SHAKE and RATTLE Algorithm for Rigid Water Models. *J. Comput. Chem.* **1992**, *13* (8), 952–

962.

(78) Kräutler, V.; Van Gunsteren, W. F.; Hünenberger, P. H. A Fast SHAKE Algorithm to Solve Distance Constraint Equations for Small Molecules in Molecular Dynamics Simulations. *J. Comput. Chem.* **2001**, *22* (5), 501–508.

(79) Ryckaert, J. P.; Ciccotti, G.; Berendsen, H. J. C. Numerical Integration of the Cartesian Equations of Motion of a System with Constraints: Molecular Dynamics of n-Alkanes. *J. Comput. Phys.* **1977**, *23* (3), 327–341.

(80) Tao, P.; Wu, X.; Brooks, B. R. Maintain Rigid Structures in Verlet Based Cartesian Molecular Dynamics Simulations. *J. Chem. Phys.* **2012**, *137* (13).

(81) Hess, B.; Bekker, H.; Berendsen, H. J. C.; Fraaije, J. G. E. M. LINCS: A Linear Constraint Solver for Molecular Simulations. *J. Comput. Chem.* **1997**, *18* (12), 1463–1472.

(82) Edition, F. Silica , Crystalline (Respirable Size). **1997**, No. Niosh 1981.

(83) Wazamtu, I.; Sani, N. A.; Abdulsalam, A. K. Extraction and Quantification of Silicon From Silica Sand Obtained From Zauma River, Zamfara State, Nigeria. *Eur. Sci. J.* **2013**, *9* (15), 160–168.

(84) Yuan, F.; Huang, L. A-B Transformation and Disorder in B-Cristobalite Silica. *Phys. Rev. B - Condens. Matter Mater. Phys.* **2012**, *85* (13), 1–7.

(85) Xie, X.; Cheng, Y.; Wu, K.; Xiao, B. Study on α-β Quartz Phase Transition and Its Effect on Dielectric Properties. *J. Appl. Phys.* **2012**, *111* (10).

(86) Wilson, M. J. The Structure of Opal-CT Revisited. *J. Non. Cryst. Solids* **2014**, *405*, 68–75.

(87) Benmore, C. J.; Soignard, E.; Amin, S. A.; Guthrie, M.; Shastri, S. D.; Lee, P. L.; Yarger, J. L. Structural and Topological Changes in Silica Glass at Pressure. *Phys. Rev. B - Condens. Matter Mater. Phys.* **2010**, *81* (5), 1–5.

(88) Chaipanich, A. Dielectric and Piezoelectric Properties of PZT-Silica Fume Cement Composites. *Curr. Appl. Phys.* **2007**, *7* (5), 532–536.

(89) Turnbull, D.; Cohen, M. H. Concerning Reconstructive Transformation and Formation of Glass. *J. Chem. Phys.* **1958**, *29* (5), 1049–1054.

(90) Veeramalai, G. Integer Interval Value of Euler'S Method for First Order Ode. **2018**, *118* (20), 2485–2490.

(91) Gleim, T. Velocity-Verlet-like Algorithm for Simulations of Stochastic Dynamics. **2009**.

(92) Matebese, B. T.; Withey, D. J.; Banda, M. K. Application of the Leapfrog Method to Robot Path Planning. *2014 IEEE Int. Conf. Inf. Autom. ICIA 2014* **2014**, No. January 2017, 710–715.

(93) Anzalone, E.; Chai, P. Numerical Integration Techniques in Orbital Mechanics Applications. **2015**, No. August, 1–14.

(94) Ozcelik, H. G.; Sozen, Y.; Sahin, H.; Barisik, M. Parametrizing Nonbonded Interactions between Silica and Water from First Principles. *Appl. Surf. Sci.* **2020**, *504* (November 2019), 144359.

(95) Munetoh, S.; Motooka, T.; Moriguchi, K.; Shintani, A. Interatomic Potential for Si-O Systems Using Tersoff Parameterization. *Comput. Mater. Sci.* **2007**, *39* (2), 334–339.

(96) Plimpton, S. Fast Parallel Algorithms for Short-Range Molecular Dynamics. *Journal of Computational Physics*. 1995, pp 1–19.